



Cite this: *Green Chem.*, 2025, **27**, 15548

## Peculiar even-odd effect in semi-crystalline poly(alkylene succinate)s with a wide range of repeating unit chain lengths

Juan Torres-Rodríguez, <sup>a</sup> Antxon Martínez de llarduya, <sup>b</sup> Haritz Sardon, <sup>a</sup> Ricardo A. Pérez-Camargo <sup>\*a</sup> and Alejandro J. Müller <sup>\*a,c</sup>

A series of novel aliphatic polysuccinates was synthesized from dimethyl succinate and various linear diols, with methylene chain lengths ( $n_{\text{CH}_2}$ ) ranging from 2 to 12 in their repeating units. The synthesis used an innovative and sustainable bulk polymerization method, greatly reducing solvent use and incorporating low-toxicity catalysts. This approach has enabled the production of a diverse array of polysuccinates for the first time, as evidenced by nuclear magnetic resonance. The crystallization behavior of these materials was systematically analyzed through a combination of Differential Scanning Calorimetry—encompassing non-isothermal, isothermal, self-nucleation (SN), and successive self-nucleation and annealing experiments—as well as *in situ* synchrotron Fourier–Transform Infrared Spectroscopy (FT-IR), Wide- and Small-Angle X-ray Scattering (WAXS/SAXS), and Polarized Light Optical Microscopy (PLOM). An intriguing even–odd effect was discovered across the entire range of  $n_{\text{CH}_2}$ , with samples containing even chain lengths exhibiting superior property values compared to their odd counterparts. In the  $n_{\text{CH}_2} < 5$  region, the even–odd effect is stronger, reflected in marked differences in thermal transitions and crystallization kinetics, attributable to variations in intermolecular interactions and unit cell structures, *e.g.*, orthorhombic *versus* monoclinic. For  $n_{\text{CH}_2} > 5$ , the even–odd effect becomes less pronounced but does not reach saturation, presenting differences in thermal transitions, crystallization kinetics, and interplanar distance within the same unit cell. Remarkably, this study reports for the first time an even–odd effect in SN experiments, suggesting that the even–odd pattern in this series of polysuccinates lacks saturation, highlighting the complexity of these materials and their potential for further exploration in sustainable polymer chemistry.

Received 17th October 2025,  
Accepted 7th November 2025

DOI: 10.1039/d5gc05522a

[rsc.li/greenchem](http://rsc.li/greenchem)

### Green foundation

1. This study describes a green and efficient solvent-free bulk polymerization method to synthesize high-molecular-weight poly(alkylene succinate)s with a wide range of methylene chain lengths, enabling fine-tuning of thermal and physical properties through molecular design.
2. The method proceeds with 100% yield, uses minimal amounts of catalyst, and produces negligible waste, representing an economical and scalable route to biodegradable polyesters. These features align with key principles of green chemistry, including safer synthesis, waste minimization, and design for end-of-life degradation.
3. Further research will focus on broadening the physicochemical characterization of these materials and related copolymers—including mechanical strength, gas permeability, and biodegradability—to validate their performance in real-world applications and guide the rational design of sustainable materials for packaging, biomedical, or agricultural uses.

## 1. Introduction

The rapid evolution of science and technology has dramatically boosted the global production of synthetic polymers, driven by their remarkable versatility across various industries, including packaging, biomedicine, and construction. However, the failure to responsibly manage plastic waste at the end of its life cycle has led to a growing environmental crisis. This situation underscores the pressing need for sustainable alternatives to traditional plastics.<sup>1–3</sup>

<sup>a</sup>POLYMAT and Department of Polymers and Advanced Materials: Physics, Chemistry and Technology, Faculty of Chemistry, University of the Basque Country UPV/EHU, Paseo Manuel Lardizabal 3, 20018, Donostia-San Sebastián, Spain.

E-mail: [ricardoarpad.perez@ehu.eus](mailto:ricardoarpad.perez@ehu.eus), [alejandrojesus.muller@ehu.es](mailto:alejandrojesus.muller@ehu.es)

<sup>b</sup>Departament d'Enginyeria Química, Universitat Politècnica de Catalunya, ETSEIB, Diagonal 647, 08028 Barcelona, Spain

<sup>c</sup>IKERBASQUE, Basque Foundation for Science, Plaza Euskadi 5, 48009, Bilbao, Spain

Innovative research is increasingly focusing on biodegradable polymers that can be broken down by natural processes with the help of enzymes. These polymers decompose into biomass, carbon dioxide, and water without releasing toxic byproducts.<sup>4</sup> The broad definition of biodegradability does not specify a degradation rate or environmental conditions, which allows many polymers to be included in this category. However, newer standards require measurable mineralization rates under specific conditions, leading to debate.<sup>5</sup> Despite this, the broad definition remains the most widely accepted in both research and industrial settings.

Biodegradable polymers can come from natural, renewable resources like plants or biomass. Examples include poly(lactic acid) (PLA) and polyhydroxylalkanoates (PHAs), such as polyhydroxybutyrate (PHB), poly(hydroxybutyrate-*co*-valerate) (PHBV), and poly(hydroxyvalerate) (PHV), polyacetals (PA),<sup>6,7</sup> and polyoxalates (POX).<sup>8,9</sup> However, in the case of PLA, its slow hydrolysis causes it to be classified as industrially compostable rather than fully biodegradable.<sup>10</sup> Biodegradable polymers can also be made from non-renewable resources like petroleum or natural gas, making them synthetic polymers. Notable synthetic biodegradable polymers include poly(butylene adipate-*co*-terephthalate) (PBAT), polycaprolactone (PCL), and polybutylene succinate (PBS).<sup>5,11-14</sup>

Within this context, aliphatic polyesters have gained particular attention due to their excellent biocompatibility, non-toxicity, and inherent hydrolytic degradability conferred by ester linkages. The increasing availability of renewable monomers, such as succinic acid and lactic acid,<sup>15-17</sup> further boosts the potential of these polyesters as next-generation biodegradable or conditionally biodegradable plastics. Advances in green synthesis enable polymers like PBS to be produced from bio-based succinic acid, which can be derived from renewable feedstocks such as sucrose, glucose, and glycerol.

With diverse applications ranging from biomedical devices to food packaging, aliphatic polyesters are essential in reducing the environmental impact of single-use plastics, paving the way toward a more sustainable future.<sup>18</sup> Among this family, PCL, PLA, and PBS are the most prominent commercial examples. These polymers are semi-crystalline and show a wide range of crystallization and melting temperatures, degrees of crystallinity ( $X_c$ ), degradation rates, permeability, processability, and mechanical performance.<sup>19,20</sup>

Notably, PBS combines a relatively high melting temperature with mechanical toughness, unlike PLA, which is more brittle. This balance enables PBS to meet application needs where PLA's fragility is a limitation, broadening the range of functional biodegradable polymers. The availability of multiple complementary biodegradable materials—each with distinct property profiles—provides practical and versatile alternatives to conventional non-biodegradable plastics. However, PBS's relatively high  $X_c$  can slow hydrolytic degradation, posing a key challenge for its wider adoption.

Researchers have employed various strategies to enhance the properties of PBS-based materials, such as blending, copolymerization, and the incorporation of fillers. Since the succi-

nate moiety is critical in imparting many favorable properties to PBS, chain length modifications could offer a broader spectrum of properties, including accelerated degradation. For instance, polyethylene terephthalate (PET) is a widely used polymer for beverage bottles, textiles, and other applications, whereas polybutylene terephthalate (PBT), differing in only 2  $\text{CH}_2$  units, is more flexible and possesses faster crystallization, finding applications in automotive parts, consumer goods, among others.<sup>21</sup> This reveals a distinct performance difference between PET and PBT, resulting from adding just two methylene units. Another interesting example is poly(3-hydroxybutyrate) (P3HB), which exhibits a melting temperature ( $T_m$ ) of around 175 °C. In contrast, poly(4-hydroxybutyrate) (P4HB), with only one additional  $\text{CH}_2$  unit, has a  $T_m$  of around 60 °C, similar to that of PCL. Despite the promising potential for developing high-performance materials through this approach, *i.e.*, modifications of the chain length, such changes have yet to be thoroughly explored within the polysuccinate family. Furthermore, from the crystallization behavior perspective, repeating unit chain length variations may give rise to intriguing phenomena, such as the even-odd effect, which can influence the material's overall performance.

The even-odd effect, as recently reviewed,<sup>20</sup> refers to the alternation of solid-state properties, such as melting and crystallization ( $T_c$ ) temperatures, crystallization kinetics,<sup>22-25</sup> as well as mechanical<sup>26,27</sup> and optical<sup>28</sup> properties, based on whether the chain length ( $n_{\text{CH}_2}$ ) is even or odd. Generally, the properties of even-numbered  $\text{CH}_2$  chains are higher than those of odd-numbered ones, impacting chain packing within crystals and altering thermal transitions and unit cell parameters. While liquid state properties, like boiling points, increase linearly with  $n_{\text{CH}_2}$ , the influence of the even-odd effect is particularly noted in thermotropic liquid crystalline phases, *n*-alkanes, and specific functionalized compounds. This effect is less studied in aliphatic linear polymers due to its weaker manifestation and limited research on polymer families with extensive  $\text{CH}_2$  units. In recent years, the molecular origins of the even-odd effect have been explored for several polymer families, such as polyethers,<sup>23-25,29</sup> polycarbonates,<sup>22,30</sup> polyamides,<sup>31,32</sup> but only a few reported cases are related to the even-odd effect in aliphatic polyesters.<sup>24,25,33</sup>

In aliphatic polyesters, recent investigations have highlighted the influence of modifications in the diacid and/or diol components on polymer properties. A notable study by Soccio *et al.*<sup>24</sup> examined polyesters synthesized from 1,3-propandiol and aliphatic dicarboxylic acids of varying chain lengths (with  $n_{\text{CH}_2}$  values of 2, 3, 4, and 7), revealing a distinct odd-even effect in their findings. Similarly, Lu *et al.*<sup>33</sup> explored polyesters derived from 1,5-pentanediol and aliphatic diacids ranging from  $n_{\text{CH}_2} = 2$  to 10, *i.e.*, 2 to 4, 7, 8, and 10, where they observed an even-odd effect. In both studies, the acid component of the repeating unit was varied while maintaining a constant diol, underscoring the significant role of diol chain length, even as similar variations in the diacid part were employed. Notably, the maximum consecutive variation of  $n_{\text{CH}_2}$  reported in these works spanned from 2 to 4, encompass-

ing only three consecutive polymers. In addition, Pan *et al.*<sup>34</sup> recently studied long-space aliphatic polyesters, which are typically sustainable polyethylene-like polymers, keeping the ethylene glycol part constant and varying the diacid part with  $n_{\text{CH}_2} = 9$  to 18, obtaining an even–odd effect. However, their study aimed to form hexagonal and orthorhombic crystals when the samples were quenched from the melt to different crystallization temperatures. A similar approach, in the sense of using high  $n_{\text{CH}_2}$ , has been employed by Alamo *et al.*<sup>35</sup> using aliphatic polyesters denoted as PEX, Y, where X is the  $n_{\text{CH}_2}$  in the diol part and Y in the diacid part for studying their crystallization rate minima. In these materials, an even–odd effect was observed when Y was 12 and 18, and X was varied between 2 and 6. In contrast, the increase in thermal transitions was linear for X = 10, 12, and 18. However, in this case, the lack of an odd number of  $n_{\text{CH}_2}$  makes it difficult to conclude whether the even–odd effect is saturated beyond X > 6.

Conversely, a different approach involves varying the length of the aliphatic diol while keeping a consistent succinic acid unit, a strategy used in this study. Papageorgiou and Bikiaris<sup>25</sup> synthesized polysuccinates using diols with  $n_{\text{CH}_2}$  values of 2, 3, and 4. They observed a strong even–odd effect, with slower crystallization kinetics for poly(propylene succinate) (PPS) compared to poly(ethylene succinate) (PES) and PBS. In a later study, Bikiaris *et al.*<sup>36</sup> synthesized polysuccinates through multi-step polycondensation using diols with even  $n_{\text{CH}_2}$  values of 2, 4, 6, 8, and 10. Although these materials showed interesting properties, the odd members were not examined. As a result, the variation of  $n_{\text{CH}_2}$  values related to the even–odd effect remains limited to 2–4, revealing a research gap, since phenomena such as saturation of the even–odd effect, already seen in other aliphatic polycarbonates<sup>22,30</sup> and polyethers,<sup>23–25</sup> may not have been fully explored for polysuccinates. Therefore, there is an important need for systematic studies on polysuccinates with longer diol chains, especially considering their potential for creating high-performance polymers and random copolymers,<sup>37,38</sup> as recently shown by Safari *et al.*<sup>39</sup>

In the present work, the synthesis of aliphatic polyesters from dimethyl succinate and linear diols with methylene chain lengths ranging from 2 to 12 was successfully achieved. Our innovative, sustainable bulk polymerization method minimizes solvent use and employs low-toxicity catalysts, producing only harmless methanol as a byproduct. We thoroughly characterize these polyesters, focusing on their thermal properties, crystalline structures, and morphology while correlating these properties with the alkyl chain length. Notably, this research is the first systematic investigation of polysuccinates with up to 12 CH<sub>2</sub> units, including an analysis of odd-chain samples to understand the even–odd behavior better. Our findings enhance the understanding of repeating unit chain length, crystallization, and molecular ordering, paving the way for developing biobased semi-crystalline and potentially biodegradable polymers with tailored thermal and mechanical properties, thereby expanding their applications in environmentally sustainable materials science.

## 2. Experimental

### 2.1. Materials

Dimethyl succinate (DMS), 1,2-ethanediol (D2), 1,3-propanediol (D3), 1,4-butanediol (D4), 1,5-pentanediol (D5), 1,6-hexanediol (D6), 1,7-heptanediol (D7), 1,8-octanediol (D8), 1,9-nonanediol (D9), 1,10-decanediol (D10), 1,11-undecanediol (D11), 1,12-dodecanediol (D12) and titanium isopropoxide (TTT) were used without any further treatment (Sigma-Aldrich).

### 2.2. Polyesters synthesis

Synthesis of polyesters with varying methylene chain lengths was carried out *via* bulk polymerization of dimethyl succinate (DMS, 1.1 mmol) and a selected  $\alpha,\omega$ -aliphatic diol (1.0 mmol), with the diol chain ( $D_{n_{\text{CH}_2}}$ ) length ranging from  $n_{\text{CH}_2} = 2$  to 12 methylene units depending on the target polyester. The different polysuccinates will be named PE $n_{\text{CH}_2}$ , where the  $n_{\text{CH}_2}$  indicates the number of methylene units of the diol part.

The polymerization procedure consisted of two main stages. For illustrative purposes, the synthesis of poly(dodecamethylene succinate) (PE12) is described in detail. DMS and D12 were introduced into a 50 mL three-necked round-bottom flask equipped with mechanical stirring (60 rpm) and immersed in a thermostated silicon oil bath, preheated to 160 °C under a nitrogen atmosphere. Once a homogeneous melt was obtained, TTP (0.00005 mmol) was added as a catalyst. The reaction was maintained under these conditions for 3 hours. Subsequently, the temperature was gradually increased to 220 °C in 10 °C increments while progressively applying vacuum to prevent foaming and reduce the sublimation of oligomers. The final stage was conducted at 220 °C under high vacuum (10<sup>-2</sup> mbar) and continuous stirring (60 rpm) for 3 hours. After this step, the material was extracted and stored in a freezer (−4 °C). This two-step procedure was similarly applied to synthesize all other polyesters in the series, obtaining the materials listed in Table 1. More details are given in Section 3.1.

**Table 1** Sample name code and number of methylene groups in the main chain of the different samples. Molecular characteristics of the samples: number and Weight average molecular weight,  $M_n$  and  $M_w$ , respectively, and dispersity D ( $M_w/M_n$ )

Sample name	$n_{\text{CH}_2}$	Molecular weight <sup>a</sup>		
		$M_n$ (g mol <sup>−1</sup> )	$M_w$ (g mol <sup>−1</sup> )	D
PE2	2	15 600	29 150	1.9
PE3	3	21 650	41 950	2.0
PE4	4	32 700	70 300	2.2
PE5	5	33 031	61 980	1.9
PE6	6	16 568	36 603	2.2
PE7	7	50 469	90 138	1.8
PE8	8	23 050	56 900	2.5
PE9	9	31 400	84 600	2.7
PE10	10	28 050	92 050	3.3
PE11	11	28 400	62 200	2.2
PE12	12	11 950	56 200	4.7

<sup>a</sup>  $M_n$ ,  $M_w$  and D were estimated by GPC.

### 2.3. Characterization

**2.3.1. Nuclear magnetic resonance (NMR).**  $^1\text{H}$  NMR spectra were obtained using a Bruker AMX-300 NMR instrument operating at 300.1 MHz frequencies. Samples were dissolved in deuterated chloroform, with TMS as the internal reference.

**2.3.2. Gel permeation chromatography (GPC).** Molecular weights and dispersities were determined using GPC conducted at 35 °C with a Waters system equipped with a refractive index detector and poly(methyl methacrylate) (PMMA) standards. Samples were chromatographed using 0.05 M sodium trifluoroacetate–hexafluoroisopropanol (NaTFA-HFIP) as the eluent, employing a linear column packed with poly(styrene-*co*-divinylbenzene) at a flow rate of 0.5 mL min<sup>-1</sup>.

**2.3.3. Differential scanning calorimetry (DSC).** DSC experiments were performed using a PerkinElmer 8500 calorimeter equipped with a refrigerated cooling system, Intracooler 3, under a nitrogen atmosphere flow of 20 mL min<sup>-1</sup> and calibrated with high-purity indium and tin standards. All samples, with an approximate weight of 3–5 mg per sample, were hermetically sealed in standard aluminum pans to be tested in the DSC. The employed thermal protocols are described below.

### Non-isothermal experiments

Non-isothermal experiments were performed according to the following protocol: (1) Heating from room temperature to a temperature  $T = 30$  °C above the melting temperature ( $T_m$ ) (first heating) of the tested sample, and held for 3 min to erase thermal history. (2) Cooling from the melt to –40 °C at 20 °C min<sup>-1</sup>. (3) Holding the temperature at –40 °C for 1 min for stabilization or conditioning, and (4) Subsequently heating the samples (second heating) to  $T$ . The thermal transitions (crystallization and melting temperatures) and enthalpies were determined from DSC curves generated in the (2) cooling and (4) second heating steps.

The glass transition temperature ( $T_g$ ) was determined using the same protocol as above, except for the second step (2), where a ballistic cooling rate, the fastest rate of the equipment, was applied to promote the formation of a larger amorphous phase.

### Isothermal crystallization experiments

To accurately perform isothermal crystallization experiments, the minimum crystallization temperature ( $T_{c,\min}$ ) must first be determined.  $T_{c,\min}$  is defined as the lowest temperature to which the sample can be cooled from the melt without undergoing crystallization during rapid cooling (60 °C min<sup>-1</sup>). This value was measured following the standard thermal protocol (Section S1.1) developed previously,<sup>40</sup> which was recently reviewed.<sup>41</sup>

Once  $T_{c,\min}$  has been established, isothermal crystallization experiments can be conducted at temperatures equal to or higher than this threshold ( $T_c \geq T_{c,\min}$ ). The isothermal protocol involves erasing the thermal history, *i.e.*, 3 min at  $T$ , and then quenched rapidly (*i.e.*, 60 °C min<sup>-1</sup>) to the selected  $T_c$

and maintaining at this temperature until crystallization is complete. Finally, the sample is heated at 20 °C min<sup>-1</sup> to  $T$ .

The melting endotherm observed after the isothermal step corresponds exclusively to the crystals formed at the selected  $T_c$ , allowing for accurate application of the Hoffman–Weeks method. By plotting  $T_m$  as a function of  $T_c$ , the equilibrium melting temperature ( $T_m^\circ$ ) can be determined through linear extrapolation of the data.

Due to the slow crystallization rate of PE3 and PE5, a step-wise isothermal crystallization at selected  $T_c$  values was performed on these samples, as described in Section S1.2 and reviewed in ref. 41.

### Self-nucleation (SN) experiments

SN is a thermal technique used to generate self-seeds or self-nuclei within the polymer melt, thereby significantly increasing the nucleation density. Fundamentally, the most efficient nucleating agents for a polymer are fragments of its own crystals or chain segments that retain a residual chain orientation.<sup>42–44</sup>

SN experiments were conducted following a well-established protocol described in previous works.<sup>42,45</sup> The procedure involves the following steps: (1) Erasure of thermal history for 3 min at  $T$ . (2) Standardization of thermal history by cooling at 20 °C min<sup>-1</sup> to –40 °C. (3) Heating at 20 °C min<sup>-1</sup> to a selected SN temperature ( $T_s$ ). (4) Hold  $T_s$  for a SN time,  $t_s$ , of 5 min. (5) Cooling from  $T_s$  at 20 °C min<sup>-1</sup>, during which the effects of the thermal treatment at  $T_s$  are manifested. (6) Conditioning at –40 °C for 1 min. (7) A subsequent heating scan at 20 °C min<sup>-1</sup> to assess changes provoked by step (4) in the melting behavior. The selected  $T_s$  values span the full melting endotherm of the material and extend beyond the end of the melting peak ( $T_{m,\text{end}}$ ). Depending on the thermal response observed during the subsequent cooling and heating after 5 min at  $T_s$ , three main SN domains<sup>43</sup> can be identified: *Domain I*, *Domain II*, and *Domain III*, along with two subdomains, *Domain IIa* and *Domain IIb*, defined by Müller *et al.*<sup>44,46</sup> More details are provided in Section S1.3.

### Successive self-nucleation and annealing (SSA)

SSA experiments were carried out following the protocol recently reviewed by Müller *et al.*<sup>47–50</sup> Steps 1 to 6 of the SSA protocol are identical to those of the SN protocol, except for the selection of the  $T_s$ . For qualitative comparison across all samples, we applied the SSA qualitative approach, selecting the highest  $T_{s,\text{ideal}}$  among all samples, as the starting  $T_s$  for the SSA protocol.

The  $T_{s,\text{ideal}}$  corresponds to the lowest  $T_s$  within *Domain II*, *i.e.*, the  $T_s$  that induces the highest crystallization temperature without annealing. In step 7, the sample was heated to  $T_{s1} = T_{s,\text{ideal}} - 5$  °C, instead of  $T$  as in the SN protocol, thereby preserving the thermal history. This defines the fractionation window, which was 5 °C in this study, though values of 2.5 and 10 °C have also been reported.<sup>50,51</sup> It is worth noting that the time at  $T_s$ ,  $t_s = 5$  min, is the optimal time in a standard DSC, as defined previously.<sup>50,51</sup>

Subsequent fractionation steps (4 to 7) were repeated with progressively lower  $T_s$  values (e.g.,  $T_{s2} = T_{s1} - 5\text{ }^\circ\text{C}$ ,  $T_{s3} = T_{s2} - 5\text{ }^\circ\text{C}$ , etc.) until the full melting range was covered (90 to  $30\text{ }^\circ\text{C}$ ). After completing the fractionation process, a final SSA heating scan was performed to reveal the resulting fractions. All heating scans were conducted at  $20\text{ }^\circ\text{C min}^{-1}$ .

Since PE3 and PE5 crystallize slowly from the melt, the samples were crystallized isothermally at  $T_c$  and then directly heated to the starting  $T_s$ , avoiding the complete melting of the crystals, representing a slight modification of the SSA protocol. However, in our discussion, we indicate that the obtained SSA final heating is employed for comparison purposes.

#### 2.3.4. Micro-differential scanning calorimetry (micro DSC).

Due to the low crystallization rates of PE3 and PE5, the non-isothermal experiments were performed using a Micro Calvet VII microcalorimeter (Setaram) equipped with a double-stage temperature control with a Peltier cooler. Hastelloy C276 vessels with an elastomer O-ring (NBR) were employed for the measurements. The sample cell was filled with the polyesters, and the reference cell was empty. The heating and cooling scans from  $-20$  to  $60\text{ }^\circ\text{C}$  were recorded at cooling rates of  $0.1\text{ }^\circ\text{C min}^{-1}$  and heating rate of  $1\text{ }^\circ\text{C min}^{-1}$ .

**2.3.5. In situ synchrotron fourier transform infrared spectroscopy (FT-IR).** *In situ* FT-IR experiments were conducted to analyze all the samples from  $4000$  to  $400\text{ cm}^{-1}$ . All samples were previously dissolved in chloroform (2 mg in 0.5 mL) and deposited in calcium fluoride ( $\text{CaF}_2$ ) plates (22 mm diameter, 0.5 mm thickness) using spin coating (Lauréll). FT-IR was performed at the BL01-MIRAS infrared beamline at the ALBA Synchrotron facility in Barcelona, Spain. A Hyperion 3000 microscope coupled to a Vertex 70 spectrometer (Bruker, Germany) was used, operating at a resolution of  $4\text{ cm}^{-1}$  with 256 co-added scans per spectrum. This setup enabled real-time, temperature-dependent measurements to investigate how conformational changes and intermolecular interactions influence crystallization behavior. FT-IR absorption spectra were recorded at  $-40\text{ }^\circ\text{C}$  using a Linkam FT-IR600 hot stage equipped with a liquid nitrogen cooling system after cooling the samples from the melt at a rate of  $20\text{ }^\circ\text{C min}^{-1}$ . For PE3 and PE5, the spectra were recorded at room temperature (RT) after a isothermal crystallization at their respective  $T_c$ .

**2.3.6. Synchrotron radiation X-ray diffraction.** *In situ* Wide- and Small-Angle X-ray Scattering (WAXS/SAXS) experiments were conducted under non-isothermal conditions at beamline BL11-NCD of the ALBA Synchrotron (Barcelona, Spain). Samples were mounted in standard DSC pans and placed within a Linkam THM600 heating stage equipped with a liquid nitrogen cooling system. The thermal protocol matched that used in the DSC measurements, as previously described. Diffraction patterns were acquired every  $1\text{ }^\circ\text{C}$  with an exposure time of 2 s and a latency of 1 s. X-rays were generated at  $12.4\text{ keV}$  ( $\lambda = 1.0\text{ \AA}$ ). For WAXS measurements, a Rayonix LX255-HS detector (active area:  $230.4 \times 76.8\text{ mm}^2$ ; pixel size:  $44\text{ }\mu\text{m}^2$ ) was positioned 15.5 mm from the sample with a tilt angle of  $27.3^\circ$ . SAXS data were also collected using a Pilatus3 1M detector (active area:  $168.7 \times 179.4\text{ mm}^2$ ;  $981 \times 1043$  pixels; pixel size:

$172 \times 172\text{ }\mu\text{m}^2$ ; frame rate: 25 frames per second) at a sample-detector distance of 6463 mm. Scattering intensity was plotted as a function of the scattering vector,  $q = 4\pi \sin \theta / \lambda$ , where  $\lambda = 1\text{ \AA}$  and  $2\theta$  is the scattering angle. Calibration was performed using chromium(III) oxide (WAXS) standards.

**2.3.7. Polarized light optical microscopy (PLOM).** A PLOM Olympus BX51, equipped with an Olympus SC50 digital camera and a Linkam TP-91 hot stage, was used to observe spherulite development. Films approximately  $10\text{ }\mu\text{m}$  thick were prepared by melting the samples between two glass slides. The samples were submitted to an isothermal protocol, such as the one used in DSC experiments, to obtain bigger spherulitic sizes. Micrographs were taken at  $T_c$  after a specific time that allowed the formation of the spherulites.

## 3. Results

### 3.1. Even-odd effect from the lowest level: synthesis procedure of polysuccinates

Fig. 1 illustrates the synthetic route for the preparation of PE12, which is used as a representative example for the polyester series. The route involves a two-step bulk polymerization process. In the first step, a transesterification reaction occurs

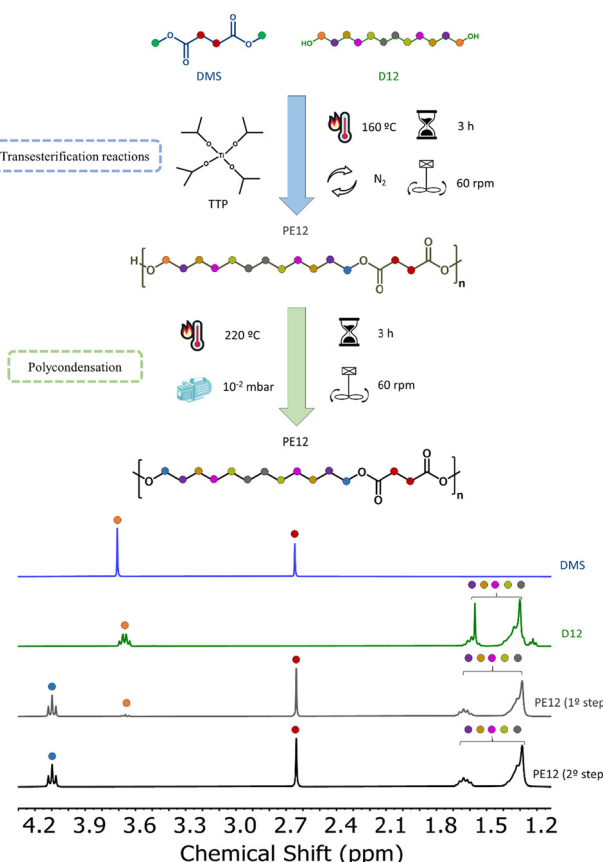


**Fig. 1** Synthetic route for the preparation of PE12. <sup>1</sup>H-NMR spectra of the DMS and D12 monomers and both PE12, before and after the polycondensation step, were included.

between DMS and D12 in a 1.1 : 1 molar ratio, respectively. The monomers were introduced into a 50 mL three-necked round-bottom flask and heated to 160 °C under a nitrogen atmosphere with mechanical stirring (60 rpm) until a homogeneous melt was obtained. TTP (0.00005 mmol) was then added as a catalyst, and the reaction proceeded under these conditions for 3 hours.

During transesterification, the  $-\text{CH}_3$  resonance from DMS at 3.70 ppm gradually decreased, indicating the formation and removal of methanol (MeOH) *via* the nitrogen purge. Concurrently, a new signal appeared at 4.10 ppm, corresponding to the  $-\text{CH}_2\text{O}-$  formed. The complete disappearance of the methyl signal and the appearance of the new  $-\text{CH}_2\text{O}-$  peak, as shown in the  $^1\text{H}$  NMR spectrum after the first reaction step (Fig. 1), confirmed the full conversion of the reaction. This quantitative conversion is particularly notable given the very low catalyst concentration used. Additionally, a signal at 3.65 ppm was attributed to the terminal  $-\text{CH}_2\text{OH}$  groups.

The second step involved polycondensation to increase the molecular weight of the resulting polyester. The temperature was gradually raised to 220 °C in 10 °C increments while progressively applying vacuum (down to  $10^{-2}$  mbar) to avoid foaming and minimize oligomer sublimation. After 3 hours under these conditions, a high-molecular-weight polymer was obtained. Fig. 1 shows the complete  $^1\text{H}$  NMR signal assignment of the polyester after the two-step reaction, presenting clear signals at 2.64 ppm and 4.10 ppm, assigned to  $-\text{CH}_2\text{COO}-$  and  $-\text{CH}_2\text{O}-$  protons, respectively. Moreover, the signals within the 1.20–1.70 ppm region were attributed to the inner methylene protons ( $-\text{CH}_2-$ ). The absence of the 3.65 ppm signal in the final spectrum reflects the effective chain extension during polycondensation, associated with high molecular weight polymers.<sup>52,53</sup>

Following this methodology, a series of aliphatic polyesters with varying methylene chain lengths were synthesized. Scheme 1 indicates the chemical modification (increase in the  $n_{\text{CH}_2}$  number) between the samples. Table 1 summarizes the polyester characteristics, showing the molecular weight values measured by GPC, all in the  $\sim 30\,000\text{ g mol}^{-1}$  range, suitable for further thermal and structural characterization.

The  $^1\text{H}$  NMR spectra of the entire series (Fig. S1) show a consistent signal at 2.64 ppm ( $-\text{CH}_2\text{COO}-$ ), while the region between 4.00–4.30 ppm varies: poly(ethylene succinate) (PE2) exhibits a singlet, attributed to the equivalent methylene proton of the ethylene glycol unit, while longer-chain polyesters display a triplet corresponding to  $-\text{CH}_2\text{O}-$  protons. As the number of methylene units increases, multiplets in the

1.20–1.70 ppm region become more prominent due to the growing  $-\text{CH}_2-$  segment content.<sup>52,53</sup> Moreover, it is appreciable that a slight difference in the chemical shift of the peaks can be associated with differences in the chain length. Fig. 2 displays the trend in chemical shifts for the two main resonances ( $-\text{CH}_2\text{O}-$  and  $-\text{CH}_2\text{COO}-$ ) across the polyester series. An even–odd effect is evident, though this trend becomes less pronounced at higher chain lengths. Still, this is our first experimental evidence of an even–odd effect and the absence of saturation for the analyzed series of polysuccinates.

**3.1.1. A greener and more efficient route for poly(alkylene succinate) synthesis.** The described polymerization approach for making polyesters with specific  $n_{\text{CH}_2}$  is eco-friendly. The reagents used, DMS and aliphatic diols, are bio-based or sustainably sourced, which helps lessen the environmental impact of the process.

In the literature, most reported synthetic routes for poly(alkylene succinates) use succinic acid (SA) as a monomer.<sup>54–58</sup> However, SA exhibits very low solubility in aliphatic diols,

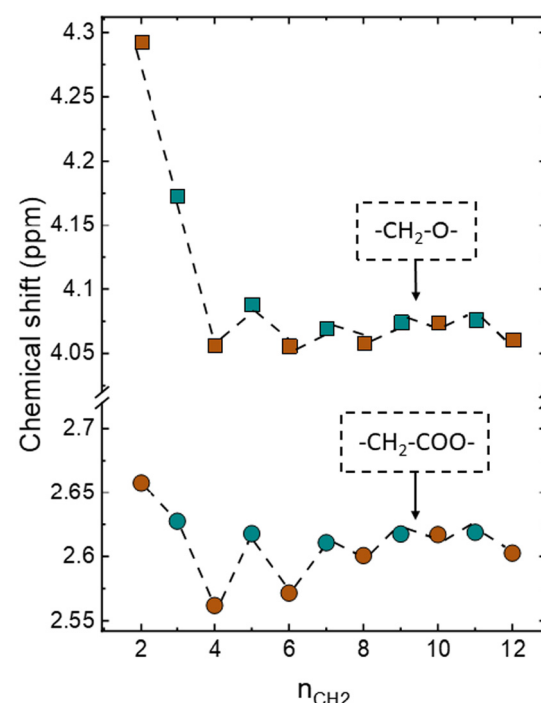
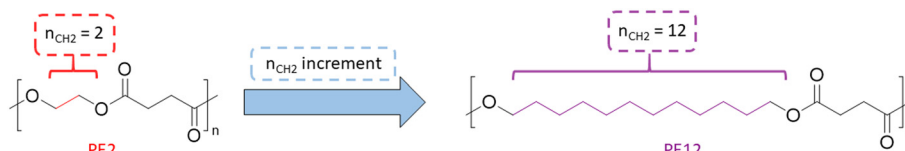


**Fig. 2** Chemical shift variation against the  $\text{CH}_2$  number in the chain of the signals attributed to  $-\text{CH}_2\text{O}-$  (4–4.3 ppm) and  $-\text{CH}_2\text{COO}-$  (2.5–2.7 ppm). A color code is used to distinguish even-numbered (brown) and odd-numbered (blue) samples.



**Scheme 1** Polyester chemical structure, indicating the part of the structure modified in the different synthesized polyesters.

causing phase separation during the reaction. Additionally, incorporating hydroxyl acid units into the main chain decreases the number of hydroxyl end-groups, which are crucial for efficient transesterification.<sup>59</sup> As a result, copolymerizations involving SA often show low polymerization efficiency.<sup>60,61</sup> Another issue with SA is that it produces water as a by-product, which negatively impacts catalyst performance<sup>62</sup> and prolongs the reaction due to the difficulty of removing water.

Using DMS instead of SA overcomes these limitations. The reaction occurs without phase separation and yields methanol as the only by-product, which is easily removed and does not affect catalyst performance. Additionally, DMS has a much lower melting temperature ( $T_m = 19^\circ\text{C}$ ) than SA ( $T_m = 185^\circ\text{C}$ ), enabling a lower reaction temperature in the first step. While polymerization with SA requires  $190^\circ\text{C}$  (ref. 54–57) or even  $225^\circ\text{C}$  (ref. 59) to fully melt the acid component, the DMS-based process works effectively at  $160^\circ\text{C}$  during this initial phase.

In addition, the stirring speed is decreased from 500 rpm, as commonly reported in the literature,<sup>55,57</sup> to 60 rpm in this work, without affecting polymer yield or quality. Klonos *et al.*<sup>63</sup> used DMS for the synthesis of PE6, PE8, and PE10; however, they performed the initial step in two consecutive heating stages ( $180^\circ\text{C}$  and  $190^\circ\text{C}$  for 2 hours each, repeated twice), achieving similar  $M_n$  but with higher energy consumption. Similarly, Shirahama *et al.*<sup>64</sup> synthesize PE4 under comparable conditions but required a higher catalyst loading (0.2% mol) to reach similar  $M_n$  values.

To evaluate the efficiency and environmental performance of our DMS-based solvent-free process, a comparison of key synthesis parameters (reaction temperature, time, stirring speed, catalyst loading, and  $M_n$ ) with relevant literature reports is included in Table S1 (Section S2). This analysis highlights the substantial reductions in energy consumption, catalyst use, and processing time achieved in this work.

In previously reported syntheses of poly(alkylene succinate), the second step is usually carried out at  $230^\circ\text{C}$  for 5 hours, resulting in a  $M_n$  of approximately  $6500\text{ g mol}^{-1}$ .<sup>55,57,65</sup> Only after extending the reaction to 20 hours at this temperature was a  $M_n$  of about  $30\,000\text{ g mol}^{-1}$  achieved.<sup>54</sup> Due to these long reaction times and high temperatures, a heat stabilizer, such as polyphosphoric acid, is often needed.

By contrast, in the synthetic route presented in this work, optimized reagent ratios and conditions enable shorter reaction times (3 hours) at a lower temperature ( $220^\circ\text{C}$ ), without using any heat stabilizer. This protocol, therefore, yields polyesters with  $M_n \sim 30\,000\text{ g mol}^{-1}$  while reducing both energy consumption and overall processing time.

Importantly, a low-toxicity catalyst was used in small amounts due to its high catalytic efficiency. Titanium (Ti) catalysts are known to outperform other organometallic (Zr, Sn, Hf, and Bi) and metal oxide (Ge and Sb) systems in PE4 synthesis.<sup>59</sup> Specifically, titanium(IV) isopropoxide was chosen for its excellent catalytic efficiency at very low concentrations, enabling rapid polycondensation while reducing metal resi-

dues. This synthesis uses lower diol/catalyst ratios (1/0.00005) than those commonly reported in the literature (1/0.002),<sup>54,64</sup> effectively reducing any potential leaching. Although catalyst recovery was not measured, the combination of minimal loading and solvent-free operation ensures a negligible environmental impact. As mentioned earlier, methanol is the only by-product, which is easily removed, resulting in a clean, low-waste process.

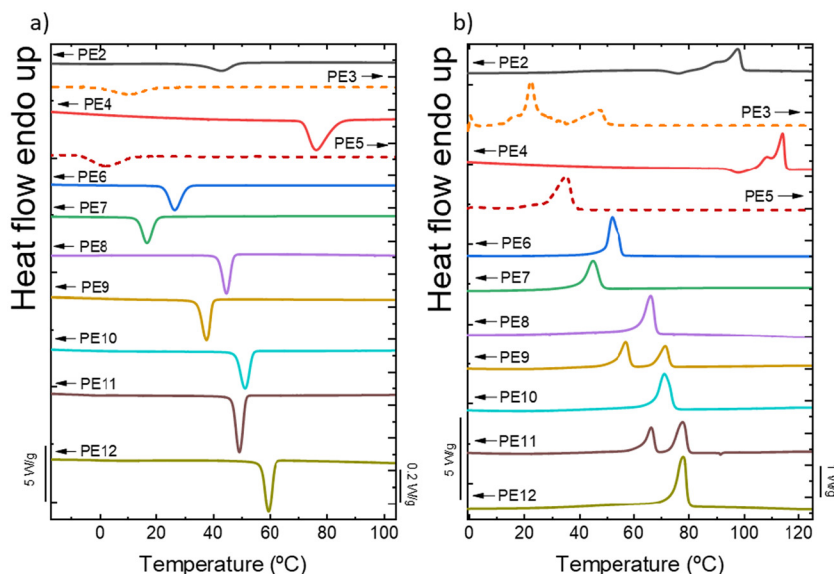
To date, only the synthesis of poly (propylene succinate) (PE3),<sup>57</sup> *i.e.*, odd-numbered, and even poly (alkylene succinate),<sup>39,54–56,58,63,64</sup> *i.e.*, PE2, PE4, PE6, PE8, and PE10 have been reported. The present work not only improves these existing routes but also extends the methodology to odd-numbered (PE5, PE7, PE9, and PE11) poly(alkylene succinate)s and PE12. This sustainable strategy enables the preparation of a wide range of polyesters, facilitating systematic studies on chain-length effects in new bio-based and potentially biodegradable materials. It should be noted, however, that the biodegradability of these polymers requires further investigation in future work.

### 3.2. Standard crystallization conditions: non-isothermal DSC

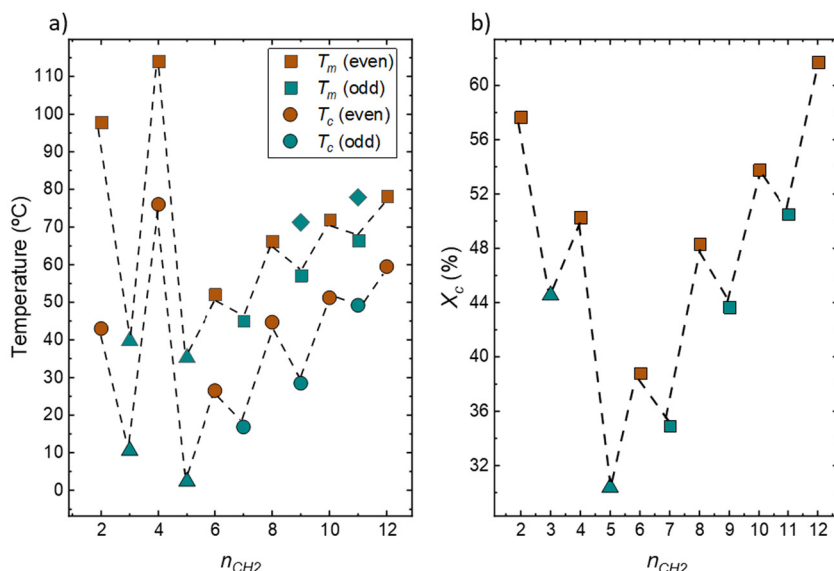
The thermal properties of the synthesized polysuccinates were investigated through non-isothermal DSC experiments. Fig. 3 displays the cooling (Fig. 3a) and second heating (Fig. 3b) DSC scans for all the samples, conducted at a  $20\text{ }^\circ\text{C min}^{-1}$  scanning rate. For comparison purposes, Fig. 3 includes PE3 and PE5 samples tested in a micro-DSC. Under standard DSC conditions, these samples cannot crystallize due to their slow crystallization. Thus, they were tested using a cooling rate of  $0.1\text{ }^\circ\text{C min}^{-1}$  and a heating rate of  $1\text{ }^\circ\text{C min}^{-1}$  in the micro-DSC. The corresponding thermal transition values are summarized in Table S2.

Fig. 3a shows that despite the slow crystallization of PE3 and PE5, all the samples can crystallize regardless of the  $n_{\text{CH}_2}$ , displaying a single  $T_c$ . This  $T_c$  does not increase as  $n_{\text{CH}_2}$  increases but instead shifts to higher or lower  $T_c$  depending on the even or odd nature of the samples. Fig. 3b shows the second heating scans, in which various samples display several endothermic and even exothermic peaks, which can be attributed to cold-crystallization, *i.e.*, PE2, and recrystallization process, *e.g.*, PE4, as shown in Fig. S2. However, in general, the main endothermic peak corresponds to the  $T_m$ , which also alternates between low and high values depending on the even or odd nature of the sample. This behavior corresponds to an even–odd effect, which is better analyzed by plotting the first-order transition temperature *versus*  $n_{\text{CH}_2}$ , as shown in Fig. 4a.

Before discussing the alternation of the thermal transitions detected in the cooling and second heating DSC scans, we will briefly discuss the nature of the additional peaks detected in the second heating DSC scans. PE2 shows an exothermic peak at low temperatures corresponding to a cold-crystallization process since not all the material was able to crystallize during the cooling step at  $20\text{ }^\circ\text{C min}^{-1}$ . Next, the following exothermic peak corresponds to a recrystallization process similar to that displayed by PE4, which is in line with the literature.<sup>66</sup> The



**Fig. 3** Non-isothermal (a) cooling and (b) subsequent heating scans for all the samples. In the case of PE3 and PE5, indicated with dashed lines, they were measured using a Calvet microcalorimeter at  $0.1\text{ }^{\circ}\text{C min}^{-1}$  cooling rate and  $1\text{ }^{\circ}\text{C min}^{-1}$  heating rate, while the rest of the samples were measured by DSC at  $20\text{ }^{\circ}\text{C min}^{-1}$  cooling and heating rate.



**Fig. 4** (a)  $T_c$  and  $T_m$  as a function of the  $n_{\text{CH}_2}$  in the repeating unit of the  $\text{PE}n_{\text{CH}_2}$ s employed. The triangles represent the data obtained by micro-DSC, while the squares and circles represent the data obtained by DSC. The rhombus symbols indicate the second melting peak in PE9 and PE11. (b)  $X_c$  variation as a function of  $n_{\text{CH}_2}$ . A color code is used to distinguish even-numbered (brown) and odd-numbered (blue) samples.

PE3 also shows multiple endothermic peaks, which are challenging to investigate due to the slow crystallization of this material, and such studies are not the aim of this article. Regarding the PE9 and PE11 samples, they show two endothermic peaks, which, according to our experimental evidence, presented in this work below by using various techniques, can be attributed to the melting of crystals at low temperatures, followed or even overlapped by a solid–solid transition that requires further investigation. Hence, despite showing the

value of each peak in Fig. 4a, we consider the first low-temperature peak to be the melting point of the crystals, while the peak at high-temperature (probably associated with a reversible solid–solid transition, see below) is plotted for reference purposes. This assignment is supported not only by experimental evidence but also by the overall trend observed throughout this work, further confirming its validity.

Fig. 4a shows the  $T_c$  and  $T_m$  vs.  $n_{\text{CH}_2}$  of the diol segment. Both thermal transitions show the typical alternation or zigzag

trend expected for an even–odd effect. In this case, polysuccinates formed by even number of  $n_{\text{CH}_2}$  exhibit higher thermal transitions than the odd-numbered counterparts.

Fig. 4a shows that the even–odd effect is not saturated despite reaching  $n_{\text{CH}_2}$  values as high as  $n_{\text{CH}_2} = 12$ . The first melting peak in PE9 and PE11 (square symbols) was considered the main fusion process of the crystals, while the second peak (rhombus symbols) corresponds to a solid–solid transition process that needs further research to be understood. Moreover, it is important to highlight that when only odd or even samples are considered, a linear increase of  $T_m$  as a function of  $n_{\text{CH}_2}$  is expected—a trend that holds when the first endothermic peak for PE9 and PE11 is used. In contrast, considering the second peak leads to a clear deviation from this expected trend, further supporting the notion that it does not correspond to a typical melting event. Nonetheless, additional analysis is required to fully understand the nature of this second peak.

Judging by the significant differences in  $T_c$  and  $T_m$ , the intermolecular interactions are stronger for  $n_{\text{CH}_2} = 2$  to 4. For  $n_{\text{CH}_2} > 4$ , the differences between transitions are lower, but the even–odd effect remains, showing an increasing trend of the  $T_c$  and  $T_m$  as  $n_{\text{CH}_2}$  increases. The absence of a saturation region may be associated with persistent and strong dipole–dipole interactions between carbonyl (C=O) groups, which continue to influence chain ordering at extended chain lengths. Moreover, considering that as the  $n_{\text{CH}_2}$  increases, the material will converge or eventually behave as a polyethylene chain, the obtained  $T_m$  are still far from that of polyethylene. Therefore, in case a saturation exists, it should be found at a much larger  $n_{\text{CH}_2}$ . This topic falls outside the scope of this article and requires further investigation. It can be considered a topic that belongs to the long-spaced polyesters, in which saturation has not been reported even with  $n_{\text{CH}_2} = 19$ .<sup>34</sup>

Using the second heating DSC scans, each sample's  $X_c$  was calculated (eqn (S1)) and plotted in Fig. 4b. As detailed in Section S3, due to the unknown equilibrium properties of most  $\text{PE}_{n_{\text{CH}_2}}$ , the equilibrium melting enthalpy was estimated using the group contribution theory of Van Krevelen.<sup>67</sup> (more details in eqn (S2) and Section S3). An even–odd trend is observed, with  $X_c$  values ranging from approximately 30 to 60%. In some cases, incorporating a single additional methylene group results in a difference in crystallinity of nearly 10%, which can significantly impact the material's ultimate properties. These results highlight the importance of studying material thermal properties, as  $X_c$  significantly affects mechanical properties, permeability, and biodegradation, impacting overall performance.

The  $T_g$  was evaluated *via* DSC following ballistic cooling (Fig. S3). The persistence of the even–odd trend in  $T_g$  values shows the high crystallization capacity of the polyesters (except PE3 and PE5). In principle, an alternation of the  $T_g$  values is not expected; however, it has been reported for PET, as its  $T_g$  values are sensitive to different factors. In general, one of these factors is the sensitivity of  $T_g$  to crystallization, which might lead to certain deviations. For polysuccinates, as is mentioned

before, there are samples with a high capacity to crystallize, which can crystallize even when ballistic cooling is employed, and thus affect the  $T_g$  values. On the other hand, samples like PE3 and PE5 cannot crystallize at a fast cooling rate; therefore, their  $T_g$  is not influenced or limited by the presence of crystals. In this context, it is important to note that cooling conditions might influence the even–odd effect observed in  $T_g$  values. Overall, polysuccinates exhibit a persistent even–odd effect of their thermal transitions and  $X_c$ , which is more pronounced for short diol segments ( $n_{\text{CH}_2} = 2$ –4), and gradually decreases but remains detectable as the chain length increases.

### 3.3. X-rays analysis

WAXS measurements were performed to gain further insights into the even–odd effect in  $\text{PE}_{n_{\text{CH}_2}}$ s. Fig. 5a shows the WAXS patterns collected at  $-40\text{ }^\circ\text{C}$  after cooling the samples from the melt at a rate of  $20\text{ }^\circ\text{C min}^{-1}$ . As PE3 and PE5 do not crystallize under these standard cooling conditions, their WAXS spectra were obtained at RT after isothermal crystallization at their respective peak  $T_c$  values obtained during slow cooling in the micro-Calorimeter.

Fig. 5 can be divided into two regions containing different WAXS patterns. For  $n_{\text{CH}_2} = 2$  to 5, the significant differences between WAXS patterns can be interpreted as originating from different unit cells, provoked by the significant differences in intermolecular interactions evidenced by FT-IR experiments shown in the next section. For example, the PE2 and PE4 possess different unit cells, *i.e.*, orthorhombic *vs.* monoclinic.

As far as we are aware, the crystalline structure of aliphatic  $\text{PE}_{n_{\text{CH}_2}}$ s has only been reported for PE2<sup>68</sup> and PE4.<sup>69</sup> Ueda *et al.*<sup>68</sup> assigned the diffraction peaks of PE2 to an orthorhombic unit cell with  $a = 7.60\text{ \AA}$ ,  $b = 10.75\text{ \AA}$ , and  $c$  (fiber axis) =  $8.33\text{ \AA}$ , with main reflections due to diffraction from (021), (121), and (200) planes. Ichikawa *et al.*<sup>69</sup> identified two different crystal unit forms in PE4, namely  $\alpha$ - and  $\beta$ -form, being both monoclinic, a different unit cell to the one reported for PE2 (orthorhombic). The  $\alpha$ -form, which is the one obtained in this work, has unit cell parameters equal to  $a = 0.523\text{ nm}$ ,  $b = 0.912\text{ nm}$ ,  $c$  (fiber axis) =  $1.090\text{ nm}$ , and  $\beta = 123.9^\circ$ , with their main peaks corresponding to the (020) and (110) planes. The  $\beta$ -form is induced only under mechanical stress, and more details can be found in ref. 69. Beyond these two examples, crystallographic information for other polysuccinates remains scarce, underscoring the need for further investigation. These structural studies are essential to fully understand structure–property relationships and will be addressed in future work. Still, Fig. 5a clearly shows that PE3 displays two main peaks at  $q$  values different from those of PE2 and PE4, while PE5 seems to possess an extra peak, which can be attributed to different unit cells. Therefore, despite having different thermal histories, there appears to be alternation of unit cells for  $n_{\text{CH}_2}$  between 2 and 5, as reported for other systems, *i.e.*, monoclinic *vs.* orthorhombic unit cells, like aliphatic polyethers and polycarbonates.<sup>22,23</sup>

For  $n_{\text{CH}_2} > 5$ , the WAXS patterns are similar, showing two main diffraction peaks. Klonos *et al.*<sup>36</sup> also found two similar

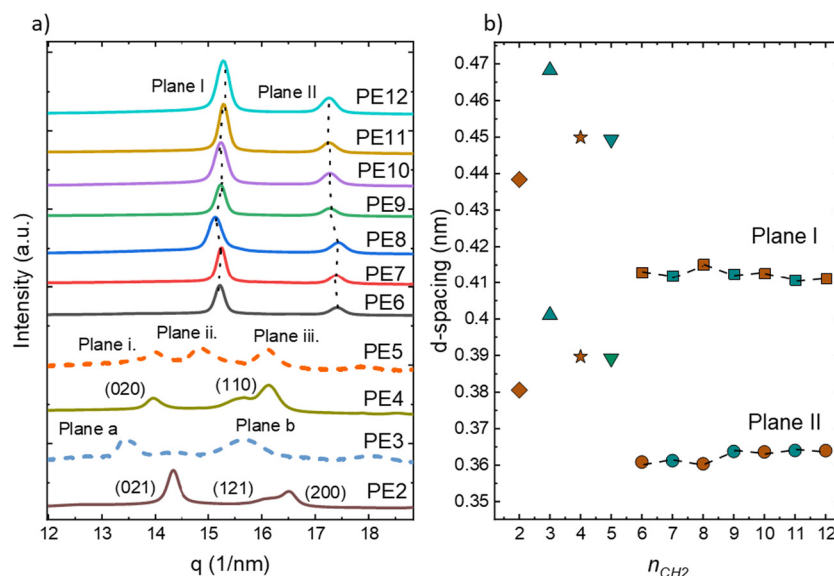


**Fig. 5** (a) WAXS patterns for all the samples. The dashed line corresponds to the WAXS patterns obtained at RT after an isothermal crystallization at their respective  $T_c$ , while the rest of the samples' WAXS patterns (solid lines) was taken at  $-40\text{ }^\circ\text{C}$  after cooling from the melt at  $20\text{ }^\circ\text{C}\text{ min}^{-1}$ . The  $q$  positions are associated with specific reported planes, as in PE2 and PE4, while those  $q$  positions that correspond to unreported planes are indicated with an arbitrary notation. (b)  $d$ -spacing as a function of  $n_{\text{CH}_2}$ . Different symbols are employed for  $n_{\text{CH}_2} < 5$ , due to the estimated  $d$ -spacing corresponding to different unit cells, while the same symbol is employed for  $d_{\text{planeI}}$  and  $d_{\text{planeII}}$  because we assumed these samples crystallize with the same unit cell. A color code is used to distinguish even-numbered (brown) and odd-numbered (blue) samples.

main diffraction peaks for PE6, PE8, and PE10, but they focused on the  $X_c$  estimations. These two diffraction peaks are similar to those exhibited by polyethylene, which crystallizes in an orthorhombic unit cell where the reflections due to scattering from the (200) and (110) crystal planes correspond to lattice spacing of 0.37 and 0.41 nm, respectively.<sup>70</sup> The crystallization in a unit cell similar to PE supports our previous hypothesis that the even–odd effect is weakened in this region, and this is probably the cause for a higher dominance of the methylene groups that possess weaker intermolecular interactions than the ester groups. In fact, in other reported systems with an even–odd effect, the appearance of a PE-like unit cell indicates the saturation region. However, in  $\text{PE}_{n_{\text{CH}_2}}$ s, despite this, Fig. 5a clearly shows that the main planes of each  $\text{PE}_{n_{\text{CH}_2}}$  vary their position depending on the even or odd nature of the polymer. This behavior is better visualized when we estimate the  $d$ -spacing values and plot them as a function of  $n_{\text{CH}_2}$  of the glycol units in Fig. 5b.

Fig. 5b shows the  $d$ -spacing values estimated using Bragg's law. Data points corresponding to PE3 and PE5, obtained *via* isothermal crystallization, are represented by triangle symbols for both reflection planes. For short alkyl chains ( $n_{\text{CH}_2} = 2$  and 4), different symbols are also employed to illustrate that the  $d$ -spacing has originated from different unit cells. Thus, for this region,  $n_{\text{CH}_2} = 2$  to 5, there is an alternation of unit cells, in line with the findings of other systems. However, in this case, further investigation is needed to determine the unit cell of these materials. Still, judging by the  $d$ -spacing, the even samples seem to be more efficiently packaged (lower  $d$ -spacing) than the odd ones, and this is reflected in their

thermal transitions and crystallization kinetics, as shown in the next section.

When  $n_{\text{CH}_2} > 5$ , the WAXS patterns shown in Fig. 5a resemble each other, indicating that the unit cell is the same; consequently, we represent the  $d$ -spacing with the same symbol. In this case, there is an alternation limited only to the  $d$ -spacing instead of between different unit cells, as shown for  $n_{\text{CH}_2} < 5$ . A PE-like unit cell was also found in long-spaced polyesters by Pan *et al.*<sup>34</sup> These authors kept the ethylene glycol part constant and varied the diacid part between  $n_{\text{CH}_2} = 9$  to 19 to obtain the long-spaced polyesters. They found the same PE-like unit cell by quenching the samples from the melt to  $T_c = 60\text{ }^\circ\text{C}$ . Differences arose when  $T_c$  of 0, 20, and  $40\text{ }^\circ\text{C}$  were used, evidencing that depending on  $n_{\text{CH}_2}$  the samples can crystallize in a hexagonal unit cell. This kind of transformation might be present in polysuccinates, but further research is required to prove this point. In any case, Pan *et al.*<sup>34</sup> do not focus their attention on the even–odd effect of the long-spaced polyesters.

Fig. 5b for  $n_{\text{CH}_2} > 5$  shows that, depending on the studied plane, the  $d$ -spacing of the even samples is higher or lower than that of the odd samples. The chain conformation in the unit cell provokes these changes. Further details in this regard are shown below in Section 3.4. Despite the differences in  $d$ -spacing for  $n_{\text{CH}_2} > 5$ , the changes are not as significant as for  $n_{\text{CH}_2} < 5$ ; however, they still lead to a considerable alternation in the properties studied in this work.

For PE9 and PE11, WAXS patterns recorded during the second heating scan at  $20\text{ }^\circ\text{C}\text{ min}^{-1}$  (Fig. S4) were analyzed to determine the source of their double endothermic peaks. Although PE9 and PE11 behave similarly, we will use PE9 as a

representative example to discuss the observed behavior. During heating, the changes in the reflection at  $q \sim 15 \text{ nm}^{-1}$  are minor, whereas for the one at  $q \sim 17 \text{ nm}^{-1}$ , in addition to a slight shift in  $q$  position, a new reflection emerges at  $q \sim 16.5 \text{ nm}^{-1}$ , at around  $56^\circ\text{C}$ , close to the temperature at which the second melting peak ends. Beyond this temperature, at  $62^\circ\text{C}$  (Fig. S4), the new reflections persist, while the original peak at  $q \sim 17 \text{ nm}^{-1}$  disappears. Subsequently, at higher temperatures, *i.e.*, near  $80^\circ\text{C}$ , all remaining reflections disappear. Although this unusual behavior requires further investigation, it appears similar to a solid-solid transition, especially since the high-temperature endothermic peak cannot be separated/fractionated, as shown in the following sections. Further details are provided in Section S4, including SAXS patterns (Fig. S5). These patterns show a single peak, indicating a monomodal distribution of lamellar thickness.

WAXS analysis shows that polysuccinates have an alternating unit cell pattern for short diol segments ( $n_{\text{CH}_2} \leq 5$ ), while longer chains form a PE-like unit cell where the even-odd effect appears as subtle differences in  $d$ -spacing.

#### 3.4. *In situ* synchrotron FT-IR analysis

The influence of the even-odd effect on the molecular conformation of the polyester chains was further explored through FT-IR at the synchrotron. Fig. 6 shows the complete FT-IR spectra, *i.e.*, 3750 to  $750 \text{ cm}^{-1}$ , for all the samples recorded at  $-40^\circ\text{C}$  after cooling from the melt at a rate of  $20^\circ\text{C min}^{-1}$ . As in WAXS measurements, PE3 and PE5 were measured at RT after undergoing isothermal crystallization at their respective

$T_c$ . The main absorption bands observed for the polyesters are marked in Fig. 6.

Characteristic signals include the asymmetric and symmetric deformation vibrations of  $-\text{CH}_2-$  groups at approximately  $2945 \text{ cm}^{-1}$  and  $1330 \text{ cm}^{-1}$ , respectively. The carbonyl stretching vibration ( $\text{C}=\text{O}$ ) appears around  $1730 \text{ cm}^{-1}$ , while the  $-\text{C}-\text{O}-\text{C}-$  and  $\text{O}-\text{C}-\text{C}-$  stretching vibrations are observed near  $1165 \text{ cm}^{-1}$  and  $1045 \text{ cm}^{-1}$ , respectively. Additional minor bands around  $3450 \text{ cm}^{-1}$  and  $920 \text{ cm}^{-1}$  can be attributed to  $-\text{C}-\text{OH}$  and terminal  $-\text{OH}$  groups. However, these are not clearly discernible due to the polymers' high molecular weight and low concentration of end groups.<sup>71-74</sup>

Notably, differences between even- and odd-numbered samples are most evident in the regions corresponding to the carbonyl stretching and the symmetric  $-\text{CH}_2-$  deformation vibrations. Considering the different unit cells for  $n_{\text{CH}_2} < 5$ , the following comparisons focus on  $n_{\text{CH}_2} > 5$  for clarity. Fig. 7 and S6 present an expanded view of the carbonyl region ( $1700$ – $1780 \text{ cm}^{-1}$ ), where the spectral shape provides insights into chain packing. More ordered and densely packed crystalline regions typically yield sharper and more defined carbonyl bands. As shown, samples with an even number of methylene groups exhibit a distinct, well-defined peak (marked with a brown arrow), whereas odd-numbered samples display either a broadened peak or a split into two less resolved peaks (marked with blue arrows). This behavior becomes less pronounced with increasing chain length, consistent with a reduction in the parity-driven effect.

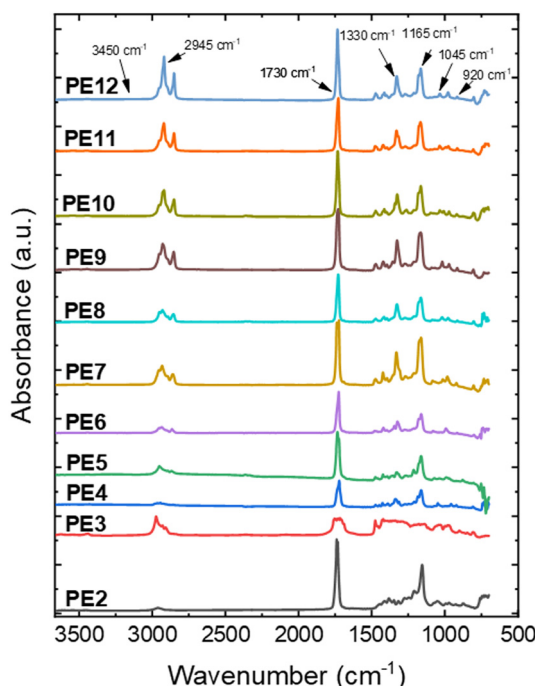


Fig. 6 Synchrotron FT-IR spectra of  $\text{PE}_{n_{\text{CH}_2}}$ s in the  $3750$ – $750 \text{ cm}^{-1}$  range at  $-40^\circ\text{C}$  after a cooling from the melt at  $20^\circ\text{C min}^{-1}$ . PE3 and PE5 spectra was obtained at RT after an isothermal crystallization.

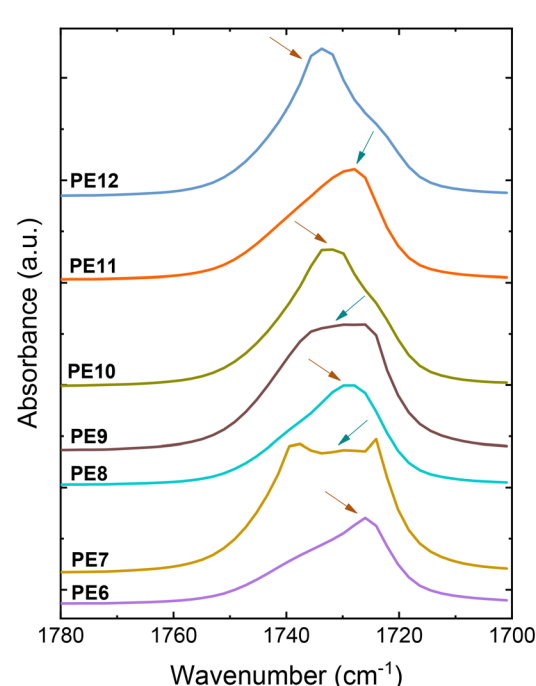
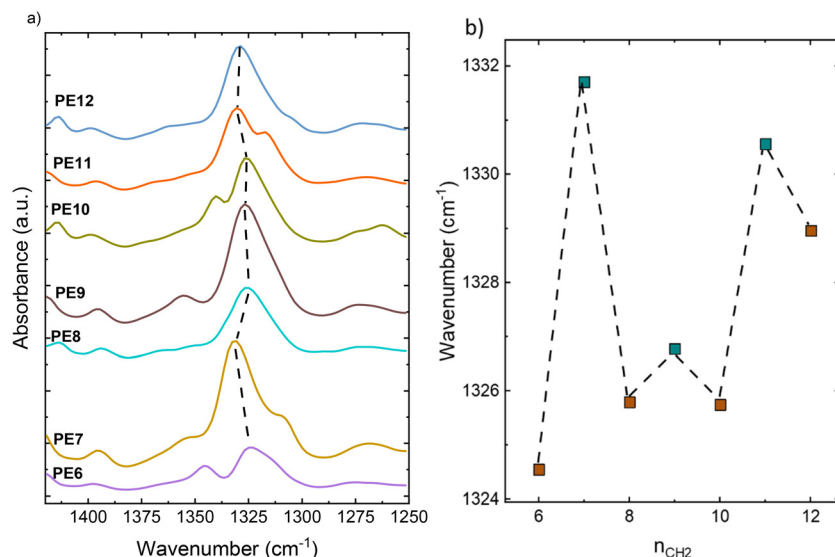


Fig. 7 Comparison of  $n_{\text{CH}_2} > 5$  samples in the carbonyl ( $\text{C}=\text{O}$ ) bands at  $-40^\circ\text{C}$  after a cooling at  $20^\circ\text{C min}^{-1}$ . The arrows indicate the main peaks.



**Fig. 8** (a) Comparison of  $n_{\text{CH}_2} > 5$  samples in symmetric deformation of the  $-\text{CH}_2-$  group bands at  $-40\text{ }^{\circ}\text{C}$  after a cooling at  $20\text{ }^{\circ}\text{C min}^{-1}$ . (b) Symmetric deformation  $-\text{CH}_2-$  peak variation as a function of  $n_{\text{CH}_2}$ . A color code is used to distinguish even-numbered (brown) and odd-numbered (blue) samples.

Fig. 8a focuses on the symmetric deformation of the  $-\text{CH}_2-$  group, centered around  $1330\text{ cm}^{-1}$ . Firstly, an increase in signal intensity is observed with increasing alkyl chain length, particularly among shorter-chain samples, likely due to a greater contribution of methylene units.

Furthermore, a shift in peak position is observed among the different samples. This trend is more clearly visualized in Fig. 8b, where it is evident that even-numbered samples (from  $n_{\text{CH}_2} = 6$  to 12) consistently exhibit peak positions at lower wavenumbers compared to their odd-numbered counterparts. In principle, this red-shift can be interpreted as stronger interactions; however, considering the groups involved, it can also indicate weaker interactions, and, therefore, less energy is needed to cause vibration. Consequently, in this case, since PE2 and PE4—with stronger interactions—show absorption bands at higher wavenumbers (Fig. S7), the shift to lower wavenumbers could be seen as a weakening of the interactions, which is more pronounced in the even samples. This trend may seem counterintuitive based on previous experiments, but it also highlights the complex behavior of the material for  $n_{\text{CH}_2} > 5$ . Overall, synchrotron FT-IR analysis demonstrates that the even–odd effect significantly influences chain conformation and packing in polyesters. Even-numbered samples display sharper carbonyl bands, indicating more ordered crystals, but also exhibit a red-shift in  $-\text{CH}_2-$  deformation, suggesting weaker intermolecular interactions when  $n_{\text{CH}_2} > 5$ .

According to the abovementioned results, it is demonstrated that the intermolecular interactions have an influence on the molecular conformation and hence their packing and crystalline structure, showing that having an even or odd  $\text{CH}_2$  number in the repeating unit could have important relevance in the microstructure and conformation of the material and thereby in their final properties and performance.

### 3.5. Crystallization kinetics: isothermal DSC measurements

The isothermal crystallization kinetics was investigated using DSC and studied through the Avrami theory.<sup>75,76</sup> The Avrami equation that includes the induction time is shown in eqn (1), following previous studies.<sup>40,41</sup>

$$1 - V_c(t - t_0) = \exp(-k(t - t_0)^n) \quad (1)$$

where  $V_c$  is the relative volumetric transformed fraction (evaluated at a specific time  $(t - t_0)$ ),  $t$  is the time of the experiment,  $t_0$  is the induction time described below,  $k$  is the overall crystallization rate constant, and  $n$  is the Avrami index, which includes contributions from nucleation and crystal growth geometry.

The isothermal curves analysis allows for obtaining information from  $t_0$ , which is, in fact, used to correctly apply the Avrami theory, and the experimental overall half-crystallization time ( $\tau_{50\%}$ ), which contains information regarding the nucleation and growth processes. The  $t_0$  is the time needed for primary nucleation before any crystallization has started,<sup>77–79</sup> and its inverse is equivalent to the initial primary nucleation rate before growth starts. The  $t_0$  and the  $\tau_{50\%}$  can be automatically obtained by using our free Crystallization Fit Origin ® APP, as reviewed in our previous work.<sup>41</sup>

Fig. 9a and b show  $1/t_0$  and the inverse of  $\tau_{50\%}$ , which is equivalent to an experimental value of the overall crystallization rate,  $1/\tau_{50\%}$ , as a function of the isothermal  $T_c$ , respectively, for all the polyesters except PE3 and PE5. These two samples exhibited extremely slow crystallization kinetics, making it unfeasible to analyze them under the standard isothermal protocol. Instead, a stepwise isothermal crystallization procedure (Section S1.2) was employed for selected  $T_c$ , as shown in Fig. S8, confirming their considerably slow crystalli-

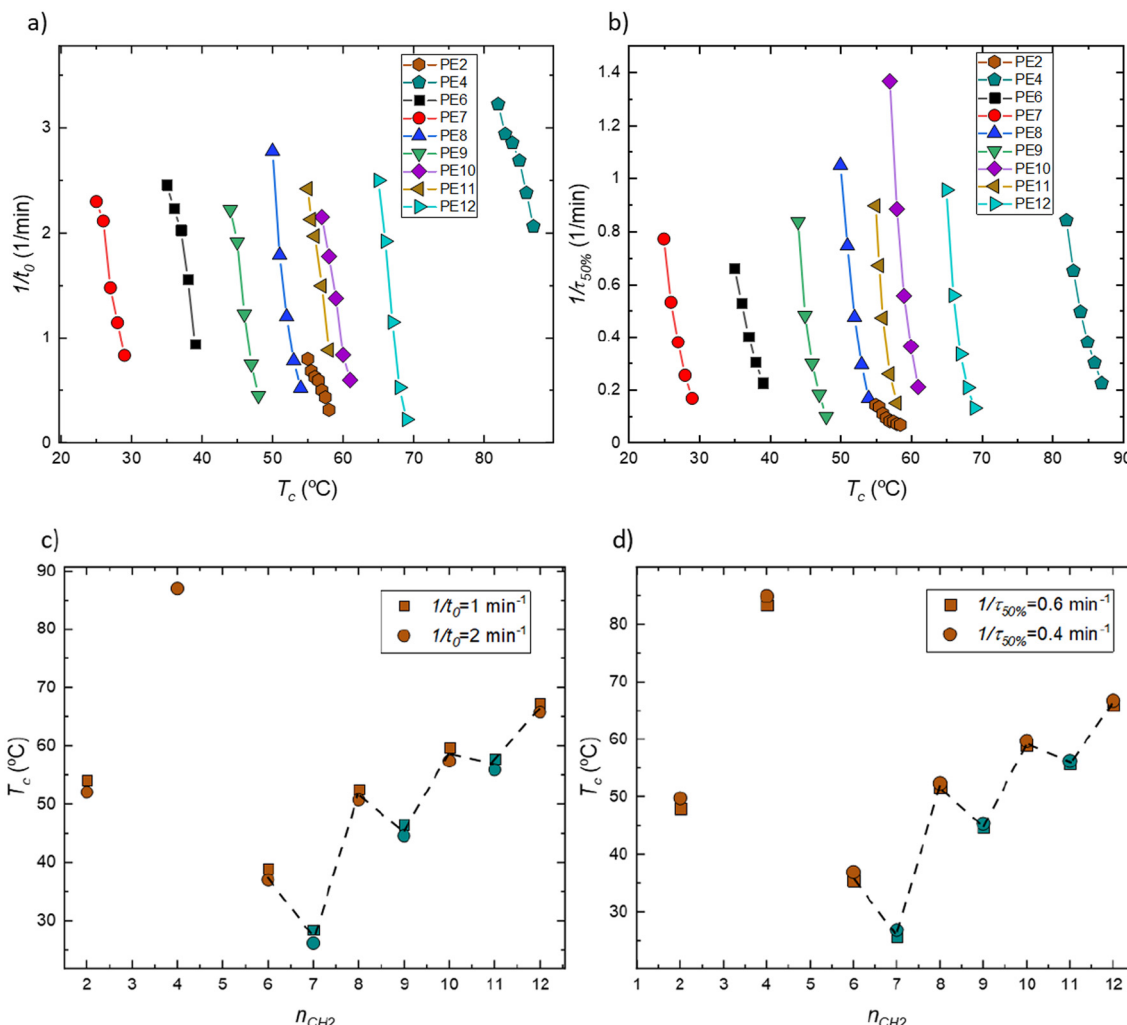


**Fig. 9** (a)  $1/t_0$  vs.  $T_c$  and (b)  $1/\tau_{50\%}$  vs.  $T_c$  obtained after isothermal crystallization. (c)  $T_c$  (at constant  $1/t_0$  value) and (d)  $T_c$  (at constant  $1/\tau_{50\%}$  value) against  $n_{CH_2}$ . A color code is used to distinguish even-numbered (brown) and odd-numbered (blue) samples.

zation behavior. For instance, for PE5, the  $\tau_{50\%}$  at  $T_c = 10.5$  °C is 150 minutes, *i.e.*,  $1/\tau_{50\%} = 0.067$  min<sup>-1</sup>; thus, performing a complete study with at least 5  $T_c$  was discarded.

Fig. 9a and b show the  $1/t_0$  and  $1/\tau_{50\%}$  vs.  $T_c$  curves for most materials (except PE3 and PE5). In this case, these polymers possess a fast crystallization rate due to their flexible nature, making it impossible to obtain data at low  $T_c$ . In polymers, for a  $1/\tau_{50\%}$  vs.  $T_c$  curve, the expected behavior is a bell-shaped behavior delimited by the  $T_g$  and  $T_m$ . This bell-shape behavior is provoked by the competition of a diffusion-controlled region at low  $T_c$  or left-hand side of the bell-shaped curve, *i.e.*, high supercooling, understood as  $\Delta T = T_m^\circ - T_c$ , in which as  $T_c$  decreases the diffusion of the chain to the growth front is difficult, due to the closeness to  $T_g$ , where the motion of the chain is practically frozen, slowing down the  $1/\tau_{50\%}$ . In contrast, at the right-hand side of the bell-shaped curve, *i.e.*, at high  $T_c$  or low  $\Delta T$ , the  $1/\tau_{50\%}$  increases as  $T_c$  decreases due to accelerated nucleation, as high  $\Delta T$  promotes higher nucleation. While close to the  $T_m^\circ$ , the  $1/\tau_{50\%}$  values are low because

of the attachment-detachment process of the chain to the growth front or extremely slow nucleation. Experimentally, for rather flexible materials, only the right side of the bell-shaped curve is obtained due to experimental limitations, *i.e.*, the cooling rates are insufficient to bypass crystallization during cooling.<sup>80-82</sup>

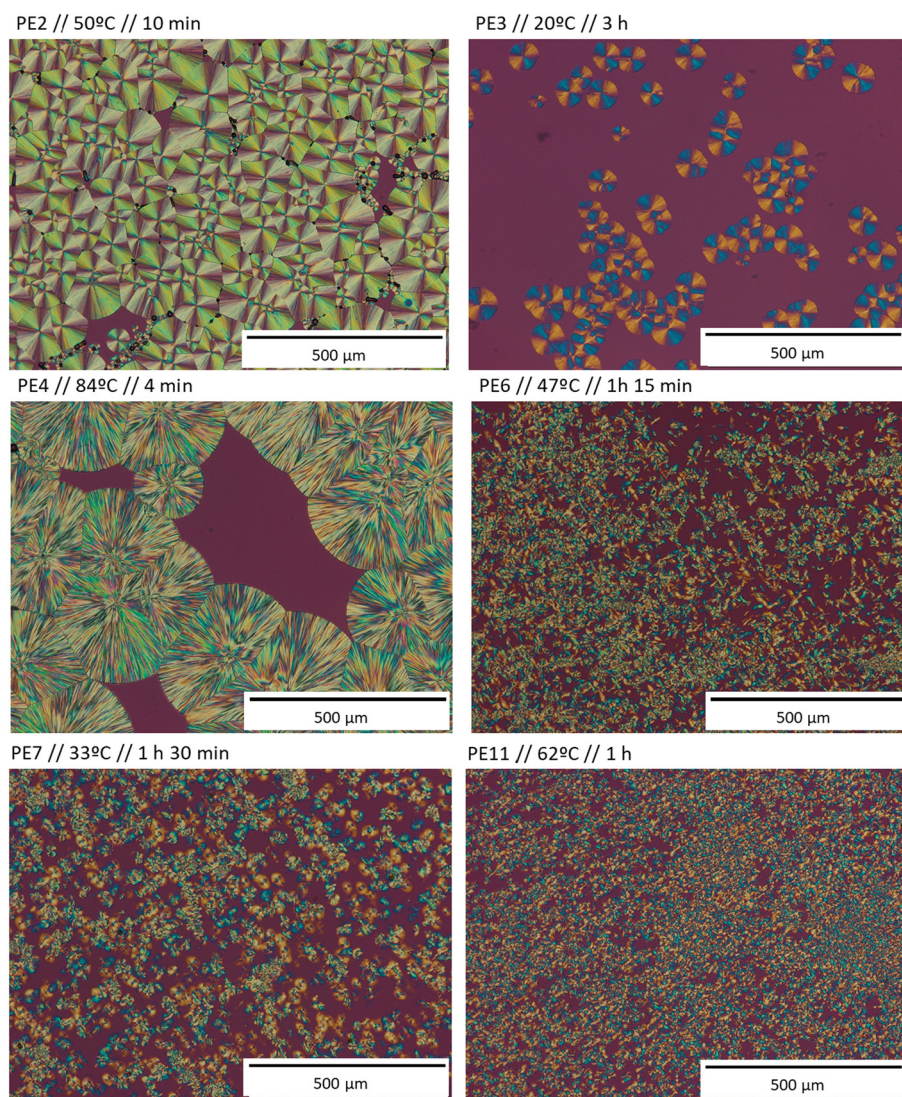
Fig. 9 shows that, as expected in the nucleation-dominated region, the  $1/t_0$  (that takes into account only primary nucleation) and  $1/\tau_{50\%}$  (that takes into account both primary and secondary nucleation after  $t_0$  has elapsed) decrease as  $T_c$  increases. When the different materials are compared, it is observed that the curves shift to higher or lower  $T_c$  depending on the evenness or nature of the studied polysuccinate. This alternation is clearly illustrated in Fig. 9c and d.

Fig. 9c compares the  $T_c$  needed to reach a constant value of  $1/t_0$  of 1.0 and 2.0 min<sup>-1</sup> as a function of  $n_{CH_2}$ , while Fig. 9d compares the  $T_c$  needed to reach a constant value of  $1/\tau_{50\%}$  of 0.4 and 0.6 min<sup>-1</sup>. These plots allow for the comparison of the effect of the  $n_{CH_2}$  on  $1/t_0$  and  $1/\tau_{50\%}$ . Fig. 9c and d show that,

despite the lack of data for PE3 and PE5, although they could probably show the lowest  $T_c$ , the values of  $T_c$  (at constant  $1/t_0$  and  $1/\tau_{50\%}$ ) are significantly higher for PE2 and PE4 than those for  $n_{\text{CH}_2} > 5$ . It can be assumed that for  $n_{\text{CH}_2} = 5$ , the  $T_c$  values will reach a minimum, as in the non-isothermal characterization. For  $n_{\text{CH}_2} > 5$ , there is an alternation of  $T_c$  vs.  $n_{\text{CH}_2}$ , with an ascending trend, evidencing that the even–odd effect is present despite the large number of methylene groups. Furthermore, lower  $T_c$  values are displayed for the polyesters with an odd number of  $\text{CH}_2$  repeating units. This evidence suggests that even samples crystallize faster than the odd ones, which may be related to their structural and conformational characteristics, as reported in other systems.<sup>22–25</sup> However, for  $n_{\text{CH}_2} > 5$ , it is worth noting that the structural and conformational changes of the polymers prepared in this work result in significant alterations to the thermal transitions and crystallization kinetics.

The even–odd trend in isothermal properties has been reported for a limited number of polymers, including polycarbonates,<sup>22</sup> polyethers,<sup>23</sup> and polyamides.<sup>32</sup> Consistent with non-isothermal results, there is no saturation of the even–odd effect under isothermal conditions. By fitting the isothermal curve with the Avrami theory (eqn (1)), we obtain information on  $n$ , which varies between 2.5 and 4 across the samples, as shown in Fig. S9a. These values suggest the formation of spherulites that are nucleated instantaneously during crystallization, as the  $n$  is close to 3, while values between 3.5 and 4 correspond to spherulites that nucleate sporadically.<sup>40,41,79,81</sup> The  $n$  does not exhibit a systematic dependence on the even–odd alternation, consistent with prior reports.<sup>22</sup> From the Avrami theory, the trend of  $K^{1/n}$  values vs.  $T_c$ , shown in Fig. S9b, is consistent with  $1/\tau_{50\%}$  vs.  $T_c$  ones, evidencing the goodness of the fitting.

Fig. 10 shows representative micrographs from PLOM experiments performed under isothermal conditions using a



**Fig. 10** PLOM micrographs acquired during isothermal crystallization from the melt for PE2, PE3, PE4, PE6, PE7, and PE11, at the indicated times and temperatures.

selected  $T_c$  for each material, confirming the presence of spherulites in all cases. Fig. S10 shows the images for all the materials.

All the materials display spherulites, which align with the obtained Avrami indexes, whose size decreases as  $n_{\text{CH}_2}$  increases. The apparent nucleation density is difficult to judge due to the differences in  $T_c$ . However, with these results, it can be hypothesized that for  $n_{\text{CH}_2} = 2$  to 5, the nucleation density is significantly higher for the even samples compared to the odd ones, a clear sign of the even–odd effect. For  $n_{\text{CH}_2} = 6$  to 12, both the spherulitic size and the nucleation density show lower variations, which is in line with DSC results, the product of the weakening of the even–odd effect.

Isothermal DSC shows that methylene parity influences crystallization rates in polysuccinates. Even-numbered chains crystallize faster due to higher nucleation, while odd-numbered chains are slower. For longer chains ( $n_{\text{CH}_2} > 5$ ), the even–odd effect continues but weakens, highlighting the role of structural and conformational factors in thermal transitions and spherulite development.

### 3.6. Melt memory and fractionation: self-nucleation (SN) and successive self-nucleation and annealing (SSA)

SN and SSA experiments were performed under the same protocol for most samples, except for PE3 and PE5 (due to their extremely slow crystallization). All samples exhibit the three SN domains during the SN test: *Domains I, II, and III*, as illustrated for selected samples in Fig. 11, which shows the cooling and heating scans after holding for 5 min at  $T_s$ . Analogous plots for all the samples are shown in Fig. S11. Interestingly, the short aliphatic chain samples PE2 and PE4 (Fig. S11a and S11b), in which the intermolecular interactions are strong, exhibit larger *Domain IIa*, which is associated with self-nuclei that persist above the melting point. As  $n_{\text{CH}_2}$  increases, *Domain IIa* decreases, as observed for PE6 and PE7. For longer methylene segments ( $n_{\text{CH}_2} > 7$ ), *Domain IIa* disappears entirely (Fig. S11c–S11i). This disappearance of *Domain IIa* is likely linked to a reduction of the strength of the interactions due to the incorporation of additional methylene units, as previously reported by Sangroniz *et al.*<sup>83</sup> These results align with those shown above, in which the differences between thermal transitions, crystallization kinetics, and unit cell for  $n_{\text{CH}_2} = 2$  to 5 were greater than those presented for  $n_{\text{CH}_2} = 6$  to 12.

Müller *et al.*<sup>43,44,83</sup> have shown that the width of *Domain IIa* is proportional to the strength of melt memory, demonstrating that *Domain IIa* depends on intermolecular interactions. In their studies on polyesters, polyamides, polycarbonates, and polyethers, they found that as the  $n_{\text{CH}_2}$  increases, melt memory, and thus the width of *Domain IIa*, decreases. In our previous work on polycarbonates,<sup>22</sup> we confirmed this behavior and further observed that *Domain IIa* appears only within the even–odd effect region. It disappears once the even–odd effect becomes saturated, corresponding to a region where intermolecular interactions are considerably weaker.

Building on these concepts, we analyzed how the widths of *Domain IIa*, *Domain IIb*, and their sum (*Domain II*) vary with

$n_{\text{CH}_2}$ , as shown in Fig. 12. Consistent with the above results, the variation in *Domain II* can be divided into two regions:  $n_{\text{CH}_2} < 5$  and  $n_{\text{CH}_2} > 5$ . In the short-chain region ( $n_{\text{CH}_2} < 5$ ), although data are missing for  $n_{\text{CH}_2} = 3$  and 5, a stronger melt memory effect is evident, reflecting more robust intermolecular interactions. In this region, *Domain II* is mainly influenced by *Domain IIa*, which is wider than *Domain IIb*. Interestingly, PE4 shows a larger *Domain II* than PE2, in line with the work of Klonos *et al.*,<sup>36</sup> deviating from the expected trend of decreasing *Domain IIa* with increasing  $n_{\text{CH}_2}$ . However, this region is difficult to interpret due to structural differences in unit cells, as discussed in Section 3.3. For  $n_{\text{CH}_2} > 5$ , the melt memory significantly decreases, although some residual memory remains, particularly for  $n_{\text{CH}_2} = 6$  and 7. However, here, *Domain II* is primarily defined by *Domain IIb*, as *Domain IIa* becomes negligible. This shift indicates a weakening of intermolecular interactions, which, based on the complete disappearance of *Domain IIa* for  $n_{\text{CH}_2} > 7$ , eventually vanish. In the specific case of PE9 and PE11, which exhibit complex thermal behavior due to a second endothermic peak associated with a solid–solid transition, only *Domain IIb* is considered present, while *Domain IIa* is absent. This is because as  $T_s$  surpassed the end of the first melting peak (low-temperature endotherm), the self-seeds can be formed from the transformed crystals, *i.e.*, solid–solid transition. Furthermore, as shown in Fig. S11f and S11h, the SN behavior of PE9 and PE11 confirms that the high-temperature endothermic peak lacks *Domain III*, supporting that this peak has a behavior that resembles a solid–solid transition.

Notably, Fig. 12 reveals that for  $n_{\text{CH}_2} > 5$ , *Domain IIb* exhibits an even–odd effect, reported here for the first time. This observation also indicates the absence of saturation of the even–odd alternation. Sangroniz *et al.*<sup>32</sup> did not observe this effect, likely because their analysis included only even-numbered polyamides. Also, Klonos *et al.*,<sup>36</sup> who only work with even polysuccinates,  $n_{\text{CH}_2} = 2, 4, 6, 8$ , and 10, could not detect this trend. Variations in a wide range of  $n_{\text{CH}_2} = 6$  to 12 in polycarbonates (including odd samples) were studied, and an alternation of *Domain II* was not observed. In the particular case of polyesters, variations in the diacid component of polyesters were made, without reaching an alternating or even–odd effect. In our case, the variation occurs in the diol segment. If only even or odd samples are analyzed independently, *Domain IIb* decreases with increasing  $n_{\text{CH}_2}$ , highlighting the importance of studying a complete set of data that includes odd and even samples. Overall, our findings suggest that the chemical nature of the polysuccinate backbone strongly affects *Domain IIb*, particularly in the odd-numbered samples, which consistently display a broader *Domain IIb* than their even-numbered counterparts. Still, further investigations are needed to understand this intriguing effect.

SSA experiments were carried out on the samples. For comparative purposes, *i.e.*, qualitative comparison approach, the highest  $T_{s,\text{ideal}}$ , corresponding to the PE4, *i.e.*,  $T_{s,\text{ideal}} = 113$  °C, was used for all the samples. PE3 and PE5 were also fractionated using the protocol described in Section 2.3.3. As illus-

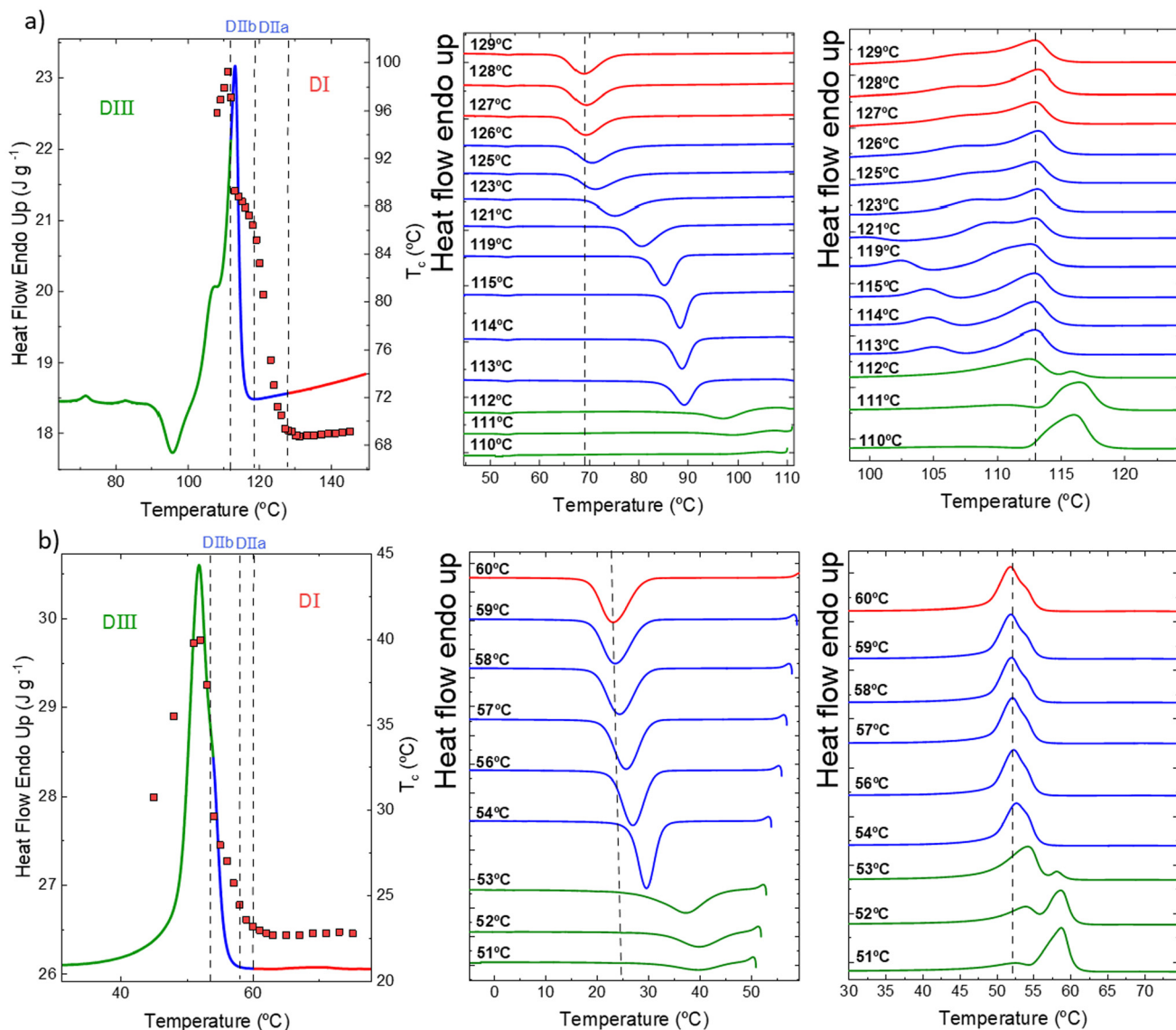


Fig. 11 DSC cooling and heating scans (at  $20\text{ }^{\circ}\text{C min}^{-1}$ ) after 5 min at the indicated  $T_s$  of (a) PE4, (b) PE6.

trated in Fig. 13a, all tested polyesters can be successfully fractionated by SSA. The employed  $T_{s,ideal}$  only cause self-nucleation in all samples, without annealing. Hence, the first thermal fraction, which is the one that melts at the highest temperature, is produced by  $T_{s1} = T_{s,ideal} - 5\text{ }^{\circ}\text{C}$ , the next fraction is created by  $T_{s2} = T_{s1} - 5\text{ }^{\circ}\text{C}$ , and so on, resulting in an SSA profile formed by the melting peaks that go from low to high temperatures.

According to previous works, SSA's best thermal fractionation results are obtained when defects (like branches, comonomers, or stereodefects) interrupt the linear crystallizable sequences, resulting in a distribution of well-resolved endothermic peaks corresponding to crystalline populations with different lamellar thicknesses.<sup>47–49,51,84–86</sup> On the other hand, molecular weight differences in homopolymers may also cause some thermal fractionation, but usually the fractions are

not so well defined. Another reason for fractionation is related to intermolecular interactions, which can be regarded as defects and hence, can also generate thermal fractionation. Therefore, sharper fractions are expected when the strength of the intermolecular interactions is higher.<sup>83</sup>

Fig. 13a presents the final DSC heating runs after SSA. The results show that all samples can be fractionated, including PE3 and PE5, for which a different SSA protocol was employed; however, their SSA profiles are still shown for comparison purposes. In most cases, the fractionation profiles display a dominant high-temperature melting fraction followed by very small secondary fractions that lack high resolution.

Interestingly, for PE7 and PE9, there is an unfractionated peak at high temperatures, as shown in Fig. 13a, that may be related to a solid–solid transition process, and this was also observed during non-isothermal experiments. The absence of

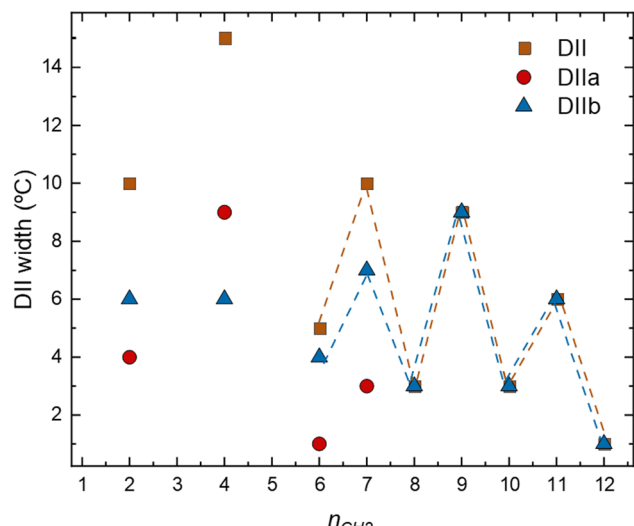


**Fig. 12** Memory effect evaluation by taking the *Domain II* variation with chain length ( $n_{\text{CH}_2}$ ).

peak fractionation associated with solid–solid transitions has been previously reported for poly(hexamethylene carbonate) and poly(octamethylene carbonate).<sup>87</sup> Moreover, it is important to highlight that solid–solid transitions, such as the Brill transition,<sup>88–91</sup> typically do not produce a detectable DSC signal and, in most cases, can only be identified through WAXS experiments. Nonetheless, the origin and nature of the solid–solid transition observed in the present study require further investigation.

For the remaining samples, the fractionation is similar. However, it is worth noting that the fractions are sharper for PE4 than for PE12, a result which could be related to the weaker intermolecular interactions in PE12. Despite the similar fractionation, the major difference between the samples lies in the temperatures at which the highest fraction melts, or the  $T_{\text{m,peak,SSA}}$ . The  $T_{\text{m,peak,SSA}}$  values are plotted as a function of  $n_{\text{CH}_2}$  in Fig. 13b, displaying an alternating or zigzag behavior. The  $T_{\text{m,peak,SSA}}$  can be regarded as an experimentally obtained  $T_{\text{m}}$  at one of the closest conditions to thermodynamic equilibrium due to the crystal perfection achieved during the successive annealing thermal treatments performed on the samples during the SSA protocol.

Fig. 13b presents the  $T_{\text{m,peak,SSA}}$ , together, for comparison purposes, with the experimental peak melting temperatures  $T_{\text{m}}$  (measured during non-isothermal DSC runs) and  $T_{\text{m}}^{\circ}$  (determined by the Hoffman–Weeks extrapolation after isothermal crystallization) versus  $n_{\text{CH}_2}$ , revealing a clear even–odd alternation in all the cases, with even-numbered polyesters consistently exhibiting higher melting points than odd-numbered ones. These results confirm the independence of the even–odd effect on the thermal history, as expected and in line with previous works.<sup>22,32</sup> As in the other experiments, the  $T_{\text{m,peak,SSA}}$  values have a larger difference (between even and odd samples) in the  $n_{\text{CH}_2} = 2$  to 5 range, and then the differences become weaker, but the melting points show a general ascending trend with  $n_{\text{CH}_2}$  in the range where  $n_{\text{CH}_2} = 6$  to 12. These trends further confirm the persistence of the even–odd effect across various thermal and morphological characterization levels and highlight the influence of chain parity on lamellar stability and thermal resistance. Moreover, these results indi-

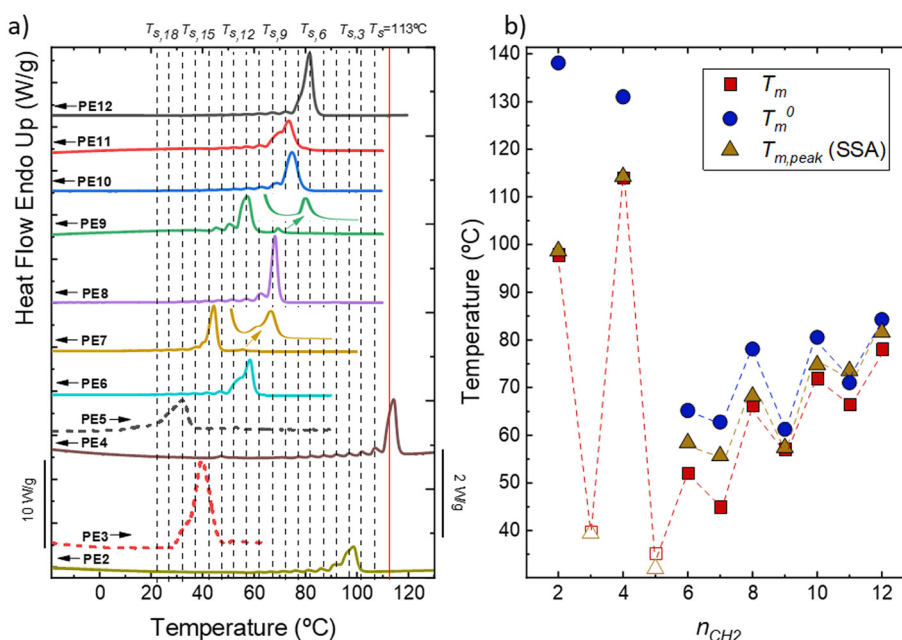


**Fig. 13** (a) Final heating after the SSA protocol was applied to the indicated samples. We used the following conditions for the SSA protocol:  $T_{\text{s,ideal}} = 113$  °C, a fractionation window of 5 °C, and scan rates of 20 °C min<sup>−1</sup>. (b)  $T_{\text{m}}$ ,  $T_{\text{m}}^{\circ}$  and  $T_{\text{m,peak}}$  (SSA) as a function of  $n_{\text{CH}_2}$ .

cate that the even–odd effect can have a subdivision between a region where intermolecular interactions are stronger and where these interactions, although present, lose strength. It can be hypothesized that with long enough  $n_{\text{CH}_2}$ , the even–odd effect will be saturated. The  $n_{\text{CH}_2}$  value, where a transition between the even–odd effect and saturation occurs, depends on the nature of the polymer. Notably, this transition occurs at  $n_{\text{CH}_2}$  around 9 in polycarbonates and polyethers, whereas in this work, no saturation is reported for  $n_{\text{CH}_2}$  as high as 12.

SN and SSA experiments demonstrate that methylene parity influences melt memory, lamellar stability, and thermal fractionation in polysuccinates. Even-numbered chains exhibit stronger interactions and higher melting points, whereas odd-numbered chains are weaker. The even–odd effect remains consistent across different chain lengths and thermal histories, although it diminishes for longer chains ( $n_{\text{CH}_2} > 5$ ).

## 4. Conclusions

In this work, we synthesized and characterized the largest series of aliphatic polysuccinates reported to date. A novel and sustainable synthesis method was developed to produce polysuccinates with varying chain lengths, from  $n_{\text{CH}_2} = 2$  to  $n_{\text{CH}_2} = 12$ . This method uses a solvent-free bulk polymerization process that eliminates volatile organic compounds and other polluting solvents. Methanol is the only byproduct, which is volatile and easily removed, enabling a clean process with minimal waste. Additionally, the monomers are either bio-based or obtained through environmentally responsible synthetic methods, reducing environmental impact from the outset. The catalyst is used in very small amounts due to its high efficiency, further minimizing catalyst-related contamination. Together, these features enhance the sustainability and environmental friendliness of the polymer synthesis route presented herein.

Across all tested crystallization conditions, the polyesters display a clear and consistent even–odd effect, visible even in samples with long aliphatic chains ( $n_{\text{CH}_2} = 12$ ). This alternation suggests that the parity of methylene and ester groups significantly influences molecular packing due to different intermolecular interactions and chain conformations, leading to the even–odd effect. Two distinct regions can be identified based on the strength of intermolecular interactions. For short alkyl chains ( $n_{\text{CH}_2} = 2$  to 5), stronger intermolecular interactions are observed, as indicated by a more pronounced even–odd effect. For longer chains ( $n_{\text{CH}_2} = 6$  to 12), interactions weaken, and although the even–odd effect still exists, the differences between even and odd samples are less distinct. These variations in interactions also impact the structure, as shown in the WAXS patterns. In the short chain region, notable differences in the WAXS patterns suggest the formation of different unit cells. As the chain length increases, the influence of methylene groups—characterized by weaker interactions—becomes more dominant over ester groups, resulting in more similar unit cells. Additionally, SN experi-

ments reveal significant differences between the two regions, with *Domain IIa* vanishing when  $n_{\text{CH}_2} > 5$ . However, despite the reduction or disappearance of interactions, *Domain IIb* behavior indicates that no saturation point was observed at high  $n_{\text{CH}_2}$  values, implying that intermolecular interactions and packing effects remain important across the entire range, even with large alkyl chains between the functional groups.

Overall, this study highlights how strategic polymer structure design, especially controlling the methylene/ester group ratio, can be used to modify the properties of polyesters. This approach paves the way for creating bio-based and potentially biodegradable materials with customizable features and enables the development of functionally optimized materials without relying on chemical additives or post-synthesis modifications, supporting more sustainable polymer processing and use. Developing high-performance materials through inherently sustainable methods strongly advances environmentally conscious polymer science.

## Author contributions

J. T.-R. conducted experiments for synthesizing and characterizing the poly(alkylene succinate)s. A. M. I. conducted the GPC experiments. J. T.-R. analyzed the data and wrote the manuscript. R. A. P.-C. and A. J. M. reviewed and edited the manuscript and supervised the work. A. J. M. was responsible for funds acquisition. A. M. I. and H. S. assisted in results discussion and reviewing the manuscript. All authors have approved the final version of the present manuscript.

## Conflicts of interest

There are no conflicts of interest to declare.

## Data availability

The data that support the findings of this study are available from the main text of the article and its supplementary information (SI). Detailed experimental procedures for  $T_{\text{c},\text{min}}$  determination, step-crystallization, and SN analyses; full synthesis conditions and molecular-weight data; comprehensive non-isothermal and isothermal DSC results with  $X_{\text{c}}$  calculations and Avrami analysis; *in situ* synchrotron WAXS/SAXS/FT-IR measurements; and PLOM micrographs and SN domain maps for PE2–PE12. See DOI: <https://doi.org/10.1039/d5gc05522a>.

More details can be obtained from the corresponding authors upon request.

## Acknowledgements

This work has received funding from the Department of Education of the Basque Government through grant no.

IT1503-22, and from the María de Maeztu Excellence Unit CEX2023-001303-M funded by MCIN/AEI/10.13039/501100011033. R. A. P.-C. is supported by the ADAGIO-H2020-MSCA COFUND-2020 program (101034379). The authors performed synchrotron radiation WAXS/SAXS experiments at BL11-NCD-SWEET (Proposal Number 2021024928) and BL-01-MIRAS beamlines (Proposal Number 2024028137) at the ALBA Synchrotron with the collaboration of ALBA staff.

## References

- 1 T. D. Nielsen, J. Hasselbalch, K. Holmberg and J. Stripple, *Wiley Interdiscip Rev Energy Environ*, 2020, **9**, 360.
- 2 D. Pan, F. Su, C. Liu and Z. Guo, *Adv. Compos. Hybrid Mater.*, 2020, **3**, 443–461.
- 3 R. Geyer, J. R. Jambeck and K. L. Law, *Sci. Adv.*, 2025, **3**, 1700782.
- 4 A. S. Luyt and S. S. Malik, in *Plastics to Energy*, ed. S. M. Al-Salem, William Andrew Publishing, 2019, pp. 403–423.
- 5 T. P. Haider, C. Völker, J. Kramm, K. Landfester and F. R. Wurm, *Angew. Chem., Int. Ed.*, 2019, **58**, 50–62.
- 6 S. Samanta, D. R. Bogdanowicz, H. H. Lu and J. T. Koberstein, *Macromolecules*, 2016, **49**, 1858–1864.
- 7 G. W. M. Vandermeulen, P. Lederhose, P. Tuzina and P. Bolduan, *Environ. Sci. Technol.*, 2025, **59**, 14444–14452.
- 8 S. Kim, K. Seong, O. Kim, S. Kim, H. Seo, M. Lee, G. Khang and D. Lee, *Biomacromolecules*, 2010, **11**, 555–560.
- 9 D. Hong, B. Song, H. Kim, J. Kwon, G. Khang and D. Lee, *Ther. Delivery*, 2011, **2**, 1407–1417.
- 10 Z. Terzopoulou, A. Zamboulis, N. D. Bikaris, E. Xanthopoulou, R. O. Ioannidis and D. N. Bikaris, *Prog. Polym. Sci.*, 2025, **167**, 101991.
- 11 R. M. Cywar, N. A. Rorrer, C. B. Hoyt, G. T. Beckham and E. Y.-X. Chen, *Nat. Rev. Mater.*, 2022, **7**, 83–103.
- 12 D. K. Schneiderman and M. A. Hillmyer, *Macromolecules*, 2017, **50**, 3733–3749.
- 13 Y. Zhu, C. Romain and C. K. Williams, *Nature*, 2016, **540**, 354–362.
- 14 Y. Zhong, P. Godwin, Y. Jin and H. Xiao, *Adv. Ind. Eng. Polym. Res.*, 2020, **3**, 27–35.
- 15 C. Vilela, A. F. Sousa, A. C. Fonseca, A. C. Serra, J. F. J. Coelho, C. S. R. Freire and A. J. D. Silvestre, *Polym. Chem.*, 2014, **5**, 3119–3141.
- 16 H. R. Kricheldorf, *Chemosphere*, 2001, **43**, 49–54.
- 17 M. Okada, *Prog. Polym. Sci.*, 2002, **27**, 87–133.
- 18 L. K. Ncube, A. U. Ude, E. N. Ogunmuyiwa, R. Zulkifli and I. N. Beas, *Recycling*, 2021, **6**, 1–25.
- 19 M. Drieskens, R. Peeters, J. Mullens, D. Franco, P. J. Lemstra and D. G. Hristova-Bogaerds, *J. Polym. Sci., Part B: Polym. Phys.*, 2009, **47**, 2247–2258.
- 20 R. A. Pérez-Camargo, J. Torres and A. J. Müller, *Polymer*, 2025, **324**, 128233.
- 21 L. De Vos, B. Van de Voorde, L. Van Daele, P. Dubrule and S. Van Vlierberghe, *Eur. Polym. J.*, 2021, **161**, 110840.
- 22 R. A. Pérez-Camargo, L. Meabe, G. Liu, H. Sardon, Y. Zhao, D. Wang and A. J. Müller, *Macromolecules*, 2021, **54**, 259–271.
- 23 I. Flores, R. A. Pérez-Camargo, E. Gabirondo, M. R. Caputo, G. Liu, D. Wang, H. Sardon and A. J. Müller, *Macromolecules*, 2022, **55**, 584–594.
- 24 M. Soccio, N. Lotti, L. Finelli, M. Gazzano and A. Munari, *Polymer*, 2007, **48**, 3125–3136.
- 25 G. Z. Papageorgiou and D. N. Bikaris, *Polymer*, 2005, **46**, 12081–12092.
- 26 C. Prisacariu and E. Scortanu, *High Perform. Polym.*, 2011, **23**, 308–313.
- 27 C. Zhou, Z. Wei, Y. Yu, S. Shao, X. Leng, Y. Wang and Y. Li, *Mater. Today Commun.*, 2019, **19**, 450–458.
- 28 D. A. M. Egbe, C. Ulbricht, T. Orgis, B. Carbonnier, T. Kietzke, M. Peip, M. Metzner, M. Gericke, E. Birckner, T. Pakula, D. Neher and U.-W. Grummt, *Chem. Mater.*, 2005, **17**, 6022–6032.
- 29 S. Kobayashi, H. Tadokoro and Y. Chatani, *Macromol. Chem. Phys.*, 1968, **112**, 225–241.
- 30 T. Masubuchi, M. Sakai, K. Kojio, M. Furukawa and T. Aoyagi, *e-J. Soft Mater.*, 2007, **3**, 55–63.
- 31 Y. Kinoshita, *Makromol. Chem.*, 1959, **33**, 1–20.
- 32 L. Sangroniz, J. L. Olmedo-Martínez, W. Hu, Y.-J. Jang, G. Liu, M. A. Hillmyer and A. J. Müller, *Biomacromolecules*, 2024, **25**, 7500–7510.
- 33 J. Lu, L. Wu and B.-G. Li, *ACS Sustainable Chem. Eng.*, 2017, **5**, 6159–6166.
- 34 M. Ding, L. Ni, Y. Zheng, B. Wang, C. Yu, G. Shan, Y. Bao, J. Liu and P. Pan, *Macromolecules*, 2025, **58**, 2005–2013.
- 35 H. Janani, C. W. Kramer, N. R. Boyd, M. Eck, S. Mecking and R. G. Alamo, *Macromolecules*, 2025, **58**, 5688–5705.
- 36 P. A. Klonos, L. Papadopoulos, M. Kasimatis, H. Iatrou, A. Kyritsis and D. N. Bikaris, *Macromolecules*, 2021, **54**, 1106–1119.
- 37 R. A. Pérez-Camargo, M. Safari, J. Torres-Rodríguez, Y. Liao and A. J. Müller, *Polymer*, 2023, **287**, 126412.
- 38 T. Debuissy, P. Sangwan, E. Pollet and L. Avérous, *Polymer*, 2017, **122**, 105–116.
- 39 M. Safari, J. Torres, R. A. Pérez-Camargo, A. Martínez de Ilarduya, A. Mugica, M. Zubitur, H. Sardon, G. Liu, D. Wang and A. J. Müller, *Biomacromolecules*, 2024, **25**, 7392–7409.
- 40 A. T. Lorenzo, M. L. Arnal, J. Albuerne and A. J. Müller, *Polym. Test.*, 2007, **26**, 222–231.
- 41 R. A. Pérez-Camargo, G.-M. Liu, D.-J. Wang and A. J. Müller, *Chin. J. Polym. Sci.*, 2022, **40**, 658–691.
- 42 B. Fillon, J. C. Wittmann, B. Lotz and A. Thierry, *J. Polym. Sci., Part B: Polym. Phys.*, 1993, **31**, 1383–1393.
- 43 L. Sangroniz, D. Cavallo and A. J. Müller, *Macromolecules*, 2020, **53**, 4581–4604.
- 44 R. M. Michell, A. Mugica, M. Zubitur and A. J. Müller, in *Polymer Crystallization I: From Chain Microstructure to Processing*, ed. F. Auriemma, G. C. Alfonso and C. de Rosa, Springer International Publishing, Cham, 2017, pp. 215–256.

45 A. J. Müller, V. Balsamo, M. L. Arnal, T. Jakob, H. Schmalz and V. Abetz, *Macromolecules*, 2002, **35**, 3048–3058.

46 L. Sangroniz, R. G. Alamo, D. Cavallo, A. Santamaría, A. J. Müller and A. Alegria, *Macromolecules*, 2018, **51**, 3663–3671.

47 A. J. Müller, Z. H. Hernández, M. L. Arnal and J. J. Sánchez, *Polym. Bull.*, 1997, **39**, 465–472.

48 A. J. Müller and M. L. Arnal, *Prog. Polym. Sci.*, 2005, **30**, 559–603.

49 A. J. Müller, R. M. Michell, R. A. Pérez and A. T. Lorenzo, *Eur. Polym. J.*, 2015, **65**, 132–154.

50 R. A. Pérez-Camargo, D. Cavallo and A. J. Müller, *Front. Soft Matter*, 2022, **2**, 1003500.

51 A. J. Müller, A. T. Lorenzo and M. L. Arnal, *Macromol. Symp.*, 2009, **277**, 207–214.

52 G. Wang, X. Hao, Y. Dong and L. Zhang, *J. Polym. Environ.*, 2023, **31**, 4990–5002.

53 K. Chrissafis, K. M. Paraskevopoulos and D. N. Bikaris, *Thermochim. Acta*, 2005, **435**, 142–150.

54 C. H. Chen, J. S. Peng, M. Chen, H. Y. Lu, C. J. Tsai and C. S. Yang, *Colloid Polym. Sci.*, 2010, **288**, 731–738.

55 K. Chrissafis, K. M. Paraskevopoulos and D. N. Bikaris, *Thermochim. Acta*, 2005, **435**, 142–150.

56 Y. Shang, X. Li, Z. Jiang and Z. Qiu, *Polym. Degrad. Stab.*, 2020, **171**, 109043.

57 K. Chrissafis, K. M. Paraskevopoulos and D. N. Bikaris, *Polym. Degrad. Stab.*, 2006, **91**, 60–68.

58 R. D. Bikaris, N. M. Ainali, E. Christodoulou, N. Nikolaidis, D. A. Lambropoulou and G. Z. Papageorgiou, *Macromol.*, 2022, **2**, 58–77.

59 N. Jacquelin, F. Freyermouth, F. Fenouillot, A. Rousseau, J. P. Pascault, P. Fuertes and R. Saint-Loup, *J. Polym. Sci., Part A: Polym. Chem.*, 2011, **49**, 5301–5312.

60 H. Azim, A. Dekhterman, Z. Jiang and R. A. Gross, *Biomacromolecules*, 2006, **7**, 3093–3097.

61 T. Debuissy, E. Pollet and L. Avérous, *Eur. Polym. J.*, 2017, **93**, 103–115.

62 M. Sokołowska, E. Stachowska, M. Czaplicka and M. El Fray, *Polym. Int.*, 2021, **70**, 514–526.

63 P. A. Klonos, L. Papadopoulos, M. Kasimatis, H. Iatrou, A. Kyritsis and D. N. Bikaris, *Macromolecules*, 2021, **54**, 1106–1119.

64 H. Shirahama, Y. Kawaguchi, M. S. Aludin and H. Yasuda, *J. Appl. Polym. Sci.*, 2001, **80**, 340–347.

65 P. Parcheta, I. Koltsov and J. Datta, *Polym. Degrad. Stab.*, 2018, **151**, 90–99.

66 M. C. Righetti, M. L. Di Lorenzo, D. Cavallo, A. J. Müller and M. Gazzano, *Polymer*, 2023, **268**, 125711.

67 D. Van Krevelen and K. Te Nijenhuis, *Properties of Polymers*, Elsevier, Amsterdam, 2009..

68 A. S. Ueda, Y. Chatani and H. Tadokoro, *Polym. J.*, 1971, **2**, 387–397.

69 Y. Ichikawa, H. Kondo, Y. Igarashi, K. Noguchi, K. Okuyama and J. Washiyama, *Polymer*, 2000, **41**, 4719–4727.

70 L. Yin, J. Chen, X. Yang and E. Zhou, *Polymer*, 2003, **44**, 6489–6493.

71 S. F. Yao, X. T. Chen and H. M. Ye, *J. Phys. Chem. B*, 2017, **121**, 9476–9485.

72 M. R. Nobile, A. Crocitti, M. Malinconico, G. Santagata and P. Cerruti, *AIP Conf. Proc.*, 2018, **1981**, 020180.

73 Y. J. Phua, W. S. Chow and Z. A. Mohd Ishak, *Polym. Degrad. Stab.*, 2011, **96**, 1194–1203.

74 Y. J. Phua, W. S. Chow and Z. A. Mohd Ishak, *eXPRESS Polym. Lett.*, 2013, **7**, 340–354.

75 M. Avrami, *J. Chem. Phys.*, 1940, **8**, 212–224.

76 M. Avrami, *J. Chem. Phys.*, 1941, **9**, 177–184.

77 M. Imai, K. Mori, T. Mizukami, K. Kaji and T. Kanaya, *Polymer*, 1992, **33**, 4457–4462.

78 F. J. Baltá-Calleja and T. A. Ezquerro, in *Encyclopedia of Materials: Science and Technology*, ed. K. H. J. Buschow, R. W. Cahn, M. C. Flemings, B. Ilschner, E. J. Kramer, S. Mahajan and P. Veyssiére, Elsevier, Oxford, 2001, pp. 7244–7252.

79 A. T. Lorenzo and A. J. Müller, *J. Polym. Sci., Part B: Polym. Phys.*, 2008, **46**, 1478–1487.

80 L. Mandelkern, *Crystallization of Polymers: Volume 2: Kinetics and Mechanisms*, Cambridge University Press, Cambridge, 2nd edn, 2004, vol. 2.

81 U. W. Gedde, *Polymer Physics*, Springer Netherlands, 1st edn, 1999.

82 J. M. Schultz, *Polymer Materials Science*, Prentice-Hall, Michigan, 1974.

83 L. Sangroniz, A. Sangroniz, L. Meabe, A. Basterretxea, H. Sardon, D. Cavallo and A. J. Müller, *Macromolecules*, 2020, **53**, 4874–4881.

84 A. T. Lorenzo, M. L. Arnal, A. J. Müller, A. Boschetti-De-Fierro and V. Abetz, *Macromol. Chem. Phys.*, 2006, **207**, 39–49.

85 I. Arandia, A. Mugica, M. Zubitur, A. Iturrospe, A. Arbe, G. Liu, D. Wang, R. Mincheva, P. Dubois and A. J. Müller, *J. Polym. Sci., Part B: Polym. Phys.*, 2016, **54**, 2346–2358.

86 A. T. Lorenzo, M. L. Arnal, A. J. Müller, M.-C. Lin and H.-L. Chen, *Macromol. Chem. Phys.*, 2011, **212**, 2009–2016.

87 R. A. Pérez-Camargo, G. Liu, L. Meabe, Y. Zhao, H. Sardon, D. Wang and A. J. Müller, *Macromolecules*, 2021, **54**, 7258–7268.

88 A. Y. Feldman, E. Wachtel, G. B. M. Vaughan, A. Weinberg and G. Marom, *Macromolecules*, 2006, **39**, 4455–4459.

89 B. Lotz, *Macromolecules*, 2021, **54**, 565–583.

90 J. Luo, T. Zhou, X. Fu, H. Liang and A. Zhang, *Eur. Polym. J.*, 2011, **47**, 230–237.

91 D. Bertoldo Menezes, A. Reyer and M. Musso, *Spectrochim. Acta, Part A*, 2018, **190**, 433–441.